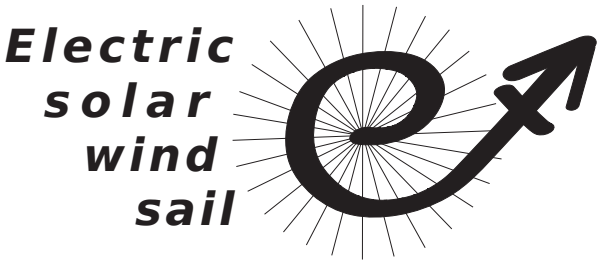

ESAIL D62.1
Summary of orbit calculations supporting WP61

Work Package: **WP62**
Version: **Version 1.0**

Prepared by: University of Pisa
G. Mengali, A. A. Quarta, G. Aliasi

Time: November 4, 2013

Coordinating person: Giovanni Mengali, g.mengali@ing.unipi.it

List of participants:

Participant no.	Participant organisation	Abbrev.	Country
8	University of Pisa	Pisa	Italy

Table of Contents

Applicable Documents

[AD1] FMI, Tartu, and Alta, “Deliverable 61.1 E-Sail mission document,” Tech. Rep. D61.1, October 2013.

[AD2] G. Mengali, A. A. Quarta, and G. Aliasi, “A graphical approach to electric sail mission design with radial thrust,” *Acta Astronautica*, vol. 82, pp. 197–208, February 2013.

[AD3] A. A. Quarta and G. Mengali, “Trajectory approximation for low-performance electric sail with constant thrust angle,” *Journal of Guidance, Control, and Dynamics*, vol. 36, pp. 884–887, May–June 2013.

[AD4] A. A. Quarta and G. Mengali, “Electric sail mission analysis for outer solar system exploration,” *Journal of Guidance, Control, and Dynamics*, vol. 33, pp. 740–755, May–June 2010.

[AD5] A. A. Quarta, G. Mengali, and P. Janhunen, “Optimal interplanetary rendezvous combining electric sail and high thrust propulsion system,” *Acta Astronautica*, vol. 68, pp. 603–621, March–April 2011.

[AD6] A. A. Quarta and G. Mengali, “Electric sail missions to potentially hazardous asteroids,” *Acta Astronautica*, vol. 66, pp. 1506–1519, May–June 2010.

[AD7] G. Mengali and A. A. Quarta, “Optimal nodal flyby with near-earth asteroids using electric sail,” in *8th IAA Symposium on the Future of Space Exploration*, (Torino, Italy), 3–5 July 2013. Submitted to Acta Astronautica.

[AD8] A. A. Quarta, G. Mengali, and P. Janhunen, “Electric sail for near-earth asteroid sample return mission: Case 1998 KY26,” *ASCE Journal of Aerospace Engineering*, (in press).

[AD9] G. Aliasi, G. Mengali, and A. A. Quarta, “Artificial equilibrium points for a generalized sail in the circular restricted three-body problem,” *Celestial Mechanics and Dynamical Astronomy*, vol. 110, pp. 343–368, August 2011.

[AD10] G. Aliasi, G. Mengali, and A. A. Quarta, “Artificial equilibrium points for a generalized sail in the elliptic restricted three-body problem,” *Celestial Mechanics and Dynamical Astronomy*, vol. 114, pp. 181–200, October 2012.

[AD11] G. Aliasi, G. Mengali, and A. A. Quarta, “Artificial equilibrium points for an electric sail with constant attitude,” *Journal of Spacecraft and Rockets*, (in press). doi: 10.2514/1.A32540.

[AD12] P. Janhunen, A. A. Quarta, and G. Mengali, “Electric solar wind sail mass budget model,” *Geoscientific Instrumentation, Methods and Data Systems*, vol. 2, no. 1, pp. 85–95, 2013.

1 Introduction

The purpose of this deliverable is to provide the necessary orbit calculations required by Electric Solar Wind Sail (E-sail) missions considered in WP 61. The basic parameters of the considered E-sail missions (target, payload mass, orbit, flight time and E-sail mass and performance) are described in deliverable [AD1]. All mathematical analyses and simulations were performed by University of Pisa, using methods and codes that have been developed for mission analysis of a spacecraft with a low-thrust propulsion system.

2 Propulsive acceleration model

The E-sail is an innovative continuous-thrust propulsion system invented in 2004 by Pekka Janhunen [1] of the Finnish Meteorological Institute.

Similar to the more known and studied photonic solar sails (see, for example, Ref. [2]), an E-sail is able to provide a continuous propulsive acceleration without using propellant. Both kinds of sails belong indeed to the category of the so called beamed-momentum propulsion systems [3], which use the momentum carried by an external stream of particles to propel the spacecraft. In particular, an E-sail exploits the high velocity stream of charged particles within the plasma (solar wind) ejected by the Sun [1,4]. The positive ions of the stream are repelled by means of Coulomb's interaction with a number of positively charged and centrifugally stretched tethers connected to the spacecraft, thus producing a net propulsive force.

Semi-analytical models and numerical simulations [4–6] suggest that the propulsive acceleration provided by an E-sail at a distance r from the Sun is proportional to $1/r^{\eta}$, where it has been estimated that $\eta \in \{1,\, 7/6\}$. More precisely, such a thrust variation with the solar distance holds true under the assumptions that: 1) the potential sheath overlapping between different tethers is negligible, 2) the available electric power varies as $1/r^2$, and 3) the employed tether voltage is independent of r. The thrust vector control capability of an E-sail based spacecraft is anyway moderate, because the thrust direction can be changed by inclining the sail nominal plane with respect to the solar wind flux (which is nearly coincident with the radial direction) within a cone whose half-width does not exceed about $35\,\mathrm{deg}$, see Fig. 1. For the purposes of the following mission analyses, an E-sail based spacecraft is modeled as a point-mass vehicle with constant mass and propulsive acceleration $\boldsymbol{a}_P$ given by

$$\boldsymbol{a}_P = a_c\,\tau \left(\frac{d}{r}\right)^{\eta} \hat{\boldsymbol{a}} \quad \text{with} \quad \alpha \triangleq \arccos\left(\hat{\boldsymbol{a}}\cdot\hat{\boldsymbol{r}}\right) \le \alpha_{\max} \tag{1}$$

where $\boldsymbol{r}$ is the Sun-spacecraft position vector with $\hat{\boldsymbol{r}} = \boldsymbol{r}/r$, d is a reference distance, usually taken equal to $1\,\mathrm{au}$, a_c, which is referred to as characteristic acceleration, is the maximum propulsive acceleration at the reference distance, $\hat{\boldsymbol{a}}$ is the unit vector of the propulsive acceleration, and $\alpha_{\max}$ is the maximum value of the sail cone α, see Fig. 1. The switching parameter $\tau \in \{0,\, 1\}$ is used in the simulations to model the on/off thrust condition for the E-sail.

Introducing an orthonormal reference frame $\mathcal{T}_{\mathrm{RTN}}(\hat{\boldsymbol{r}},\, \hat{\boldsymbol{t}},\, \hat{\boldsymbol{n}})$, the propulsive acceleration unit vector is written as

$$\hat{\boldsymbol{a}} = \cos\alpha\,\hat{\boldsymbol{r}} + \sin\alpha\,\left(\cos\delta\,\hat{\boldsymbol{t}} + \sin\delta\,\hat{\boldsymbol{n}}\right) \tag{2}$$

where $\delta \in [0,\, 360]\,\mathrm{deg}$ (called clock angle) is the angle between the direction of $\hat{\boldsymbol{t}}$ and the projection of $\hat{\boldsymbol{a}}$ onto the $(\hat{\boldsymbol{t}}, \hat{\boldsymbol{n}})$-plane. The unit vectors of the $\mathcal{T}_{\mathrm{RTN}}$ frame are

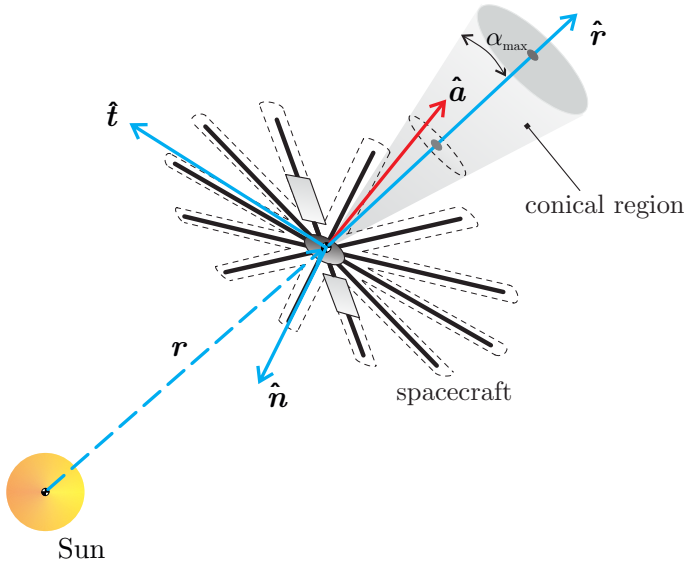

Figure 1: Spacecraft propulsive acceleration vector direction.

defined as

$$\hat{\boldsymbol{r}} = \frac{\boldsymbol{r}}{\|\boldsymbol{r}\|} \quad , \quad \hat{\boldsymbol{n}} = \frac{\boldsymbol{r} \times \boldsymbol{v}}{\|\boldsymbol{r} \times \boldsymbol{v}\|} \quad , \quad \hat{\boldsymbol{t}} = \hat{\boldsymbol{n}} \times \hat{\boldsymbol{r}} \tag{3}$$

where $\boldsymbol{v}$ is the spacecraft velocity vector.

The previous acceleration model has been adopted to study different mission scenarios for an E-sail based spacecraft. In particular, four classes of mission scenarios have been analyzed, in which the characteristic acceleration and the maximum cone angle have been selected as performance parameters.

3 Mission analysis with simplified mathematical models

Semi-analytical approaches to E-sail heliocentric mission analysis have been developed under suitable simplifying assumptions. In particular, two relevant cases are here discussed. First, the spacecraft is assumed to be subject to a purely radial, outward, propulsive acceleration [AD2]. Then, the case of a low-performance E-sail with constant thrust angle is analyzed [AD3].

3.1 E-sail motion with purely radial thrust

The potential well concept, originally introduced by Prussing and Coverstone-Carroll [7], enables a semi-analytical approach to be performed for an E-sail motion with radial thrust within a Two-Dimensional (2D) mission scenario.

Consider an E-sail whose attitude nominal plane is oriented in such a way to provide a purely radial thrust along the whole heliocentric trajectory. The propulsive acceleration is modeled according to Eq. (1) with $d \triangleq r_{\oplus} = 1\,\mathrm{au}$, $\eta = 1$, and $\alpha \equiv 0\,\mathrm{deg}$. The spacecraft is initially placed on a heliocentric parking orbit of semilatus rectum p_0 and eccentricity e_0, see Fig. 2. The E-sail propulsive system is switched-on at time $t = t_0 \triangleq 0$, at a distance r_0 from the Sun, when the spacecraft polar angle is θ_0

Due to the propulsive thrust, the specific mechanical energy $\mathcal{E}$ of the spacecraft osculating orbit varies during the motion. However, such energy is constrained to be greater than a minimum allowable value $\mathcal{E}_w$ [7].

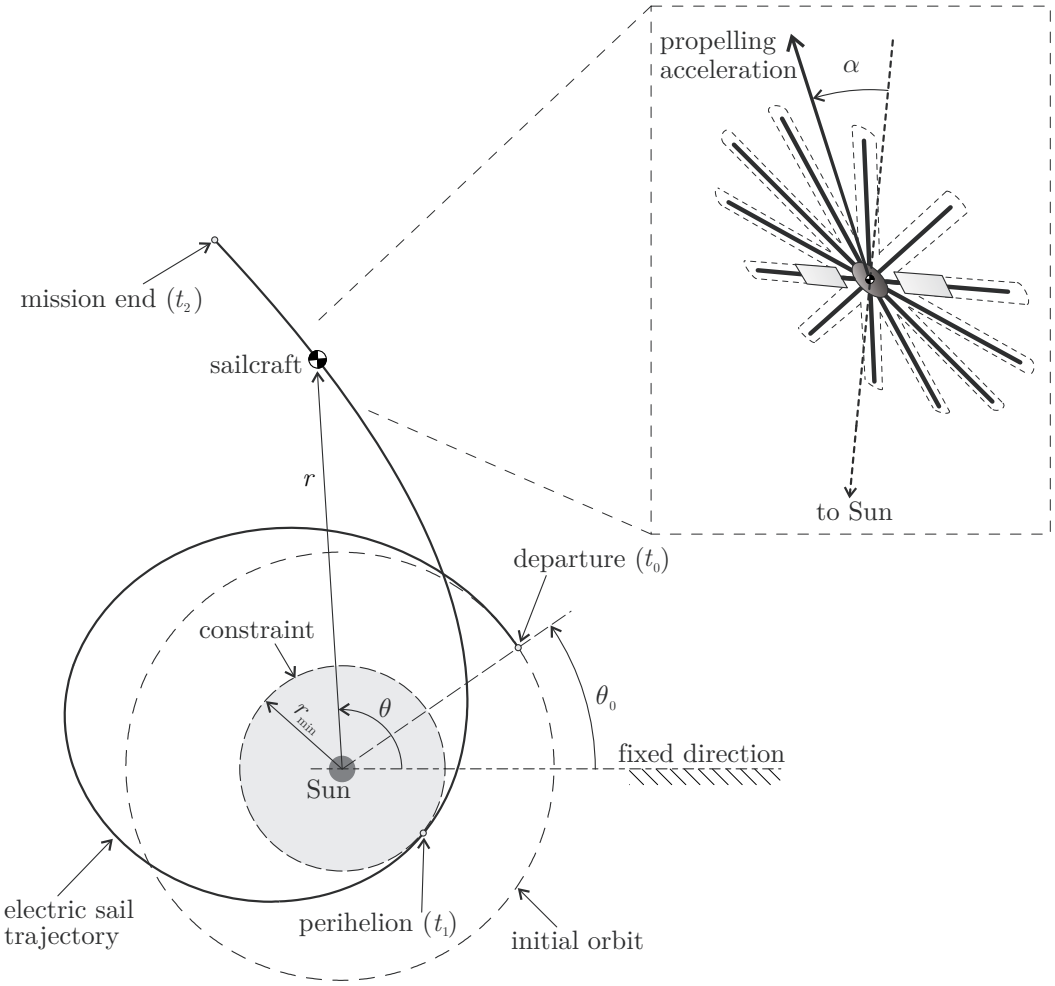

Figure 2: Polar reference frame and typical E-sail two-dimensional trajectory.

More precisely, introduce the dimensionless energies $\widetilde{\mathcal{E}}$ and $\widetilde{\mathcal{E}}_w$ such that

$$\widetilde{\mathcal{E}} \triangleq \frac{\mathcal{E}}{\mu_\odot / r_0} = \frac{e_0^2 - 1}{2\ (1 + e_0\ \cos\theta_0)} + \beta\, \frac{p_0}{r_\oplus\ (1 + e_0\ \cos\theta_0)}\, \widetilde{r} \tag{4}$$

$$\widetilde{\mathcal{E}}_w \triangleq \frac{\mathcal{E}_w}{\mu_\odot / r_0} = \frac{(1 + e_0\ \cos\theta_0)}{2}\ \exp(-2\,\widetilde{r}) - \exp(-\widetilde{r}) \tag{5}$$

where

$$\widetilde{r} \triangleq \log\left(\frac{r}{r_0}\right) \qquad , \qquad \beta = \frac{a_c}{\mu_\odot / r_\oplus^2} \tag{6}$$

and $\mu_\odot$ is the Sun’s gravitational parameter. The constraint on the minimum energy is given by

$$\widetilde{\mathcal{E}} \geq \widetilde{\mathcal{E}}_w \tag{7}$$

Equation (4) maps the spacecraft motion into the “energy plane”, that is, the plane where the osculating orbit’s specific mechanical energy $\widetilde{\mathcal{E}}$ is expressed as a function of the augmented radial distance. In this plane the spacecraft motion is from below constrained by the potential well $\widetilde{\mathcal{E}}_w$.

From Eq. (5) it is clear that the shape of the potential well boundary $\widetilde{\mathcal{E}}_w = \widetilde{\mathcal{E}}_w(\widetilde{r})$ depends both on the parking orbit characteristics (through e_0) and on the initial spacecraft position θ_0, but it is independent of the E-sail performance (quantified through

the dimensionless characteristic acceleration β). On the contrary, for a circular parking orbit ($e_0 = 0$) the function $\widetilde{\mathcal{E}}_w$ is independent of θ_0. Moreover, Eq. (4) states that the dimensionless specific mechanical energy is a linear function of $\widetilde{r}$, and its slope is proportional to β. For a circular parking orbit ($\widetilde{r} \equiv 0$), the initial value of the dimensionless specific mechanical energy is simply $\widetilde{\mathcal{E}} = -1/2$.

A graphical interpretation of Eqs. (4)-(5) provides valuable insights into the spacecraft heliocentric trajectory without the need of integrating the equations of motion. However, useful results for a preliminary mission analysis can be obtained by simply intersecting the potential well boundary with the line corresponding to the specific mechanical energy level. Applications of this methodology are discussed in Ref. [AD2].

As an example of the application of the previous concepts to an E-sail mission analysis, consider the problem of finding the minimum propulsive acceleration required to escape from the Sun starting from a circular parking orbit and assuming that the propulsion system is operating for the whole mission duration. The minimum value of a_c can be found graphically in the energy plane, assuming a circular starting orbit.

The shape of the potential well $\widetilde{\mathcal{E}}_w = \widetilde{\mathcal{E}}_w(\widetilde{r})$ for a circular parking orbit of radius $r_0 \equiv p_0$ is shown in Fig. 3. Recall that the points below the potential well boundary belong to a forbidden region (grey region in Fig. 3) where the spacecraft motion cannot take place. According to Eq. (4), at the initial time t_0 the spacecraft position

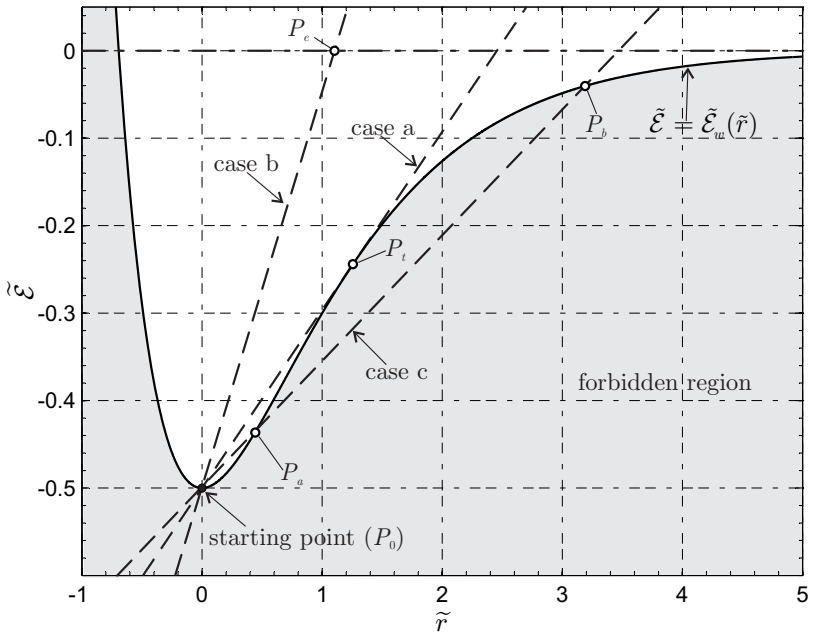

Figure 3: Potential well boundary $\widetilde{\mathcal{E}}_w = \widetilde{\mathcal{E}}_w(\widetilde{r})$ [see Eq. (5)] for a circular parking orbit.

in the energy plane is represented by the point $P_0 = (0, -1/2)$, and the spacecraft radial velocity at t_0 is zero. When the propulsion system is switched-on ($t > t_0$), the spacecraft at first increases both its specific energy $\widetilde{\mathcal{E}}$ and its distance from the Sun $\widetilde{r}$ moving along the straight line defined by Eq. (4). This line will be referred to as “energy line”, and its slope is proportional to β. The spacecraft motion corresponds to one of the following three cases.

Case a

The energy line, with a slope $\beta^\star\, r_0/r_\oplus$, is tangent to the potential well boundary at $P_t = (\widetilde{r}_t, \widetilde{\mathcal{E}}_t)$, see Fig. 3. In this case, the pair $(\widetilde{r}_t, \beta^\star)$ is solution of the system of

algebraic equations:

$$\widetilde{\mathcal{E}} = \widetilde{\mathcal{E}}_w \qquad \cap \qquad \frac{\partial \widetilde{\mathcal{E}}}{\partial \widetilde{r}} = \frac{\partial \widetilde{\mathcal{E}}_w}{\partial \widetilde{r}} \tag{8}$$

that is

$$\widetilde{r}_t \simeq 1.25643120862617 \qquad , \qquad \beta^\star \simeq 0.20363218879454 \left(\frac{r_\oplus}{r_0}\right) \tag{9}$$

The spacecraft motion can now be qualitatively described as follows. When the propulsion system is switched-on, the Sun-spacecraft distance increases following the segment $\overline{P_0 P_t}$. At time t_t the spacecraft reaches the point P_t whose distance from the Sun is $r_t \triangleq r_0 \exp(\widetilde{r}_t) \simeq 3.51286241725234\, r_0$. Here the spacecraft radial velocity is zero, because P_t belongs to the potential well boundary, while its radial acceleration is $\ddot{r}_t = 0$. Therefore, the spacecraft reaches P_t with zero velocity and zero acceleration in the radial direction. Accordingly, for $t \geq t_t$ the spacecraft tracks a circular, non-Keplerian, orbit of radius r_t with a constant velocity $v = \sqrt{\mu_\odot\, p_0}/r_t$. A linear stability analysis reveals that this non-Keplerian orbit is unstable. In other terms, a small deviation from the nominal circular orbit (due, for example, to a difference between the actual spacecraft thrust and the nominal thrust) implies a substantial time variation of the spacecraft distance from the Sun. The corresponding spacecraft trajectory resembles that shown in Fig. 4.

Case b

When the slope of the energy line is sufficiently high (that is, $\beta > \beta^\star$), P_0 is the only intersection point between the energy line and the potential well boundary, see Fig. 3. In this case, for all $t > t_0$, the spacecraft is pushed away from the Sun and eventually reaches the escape condition $\widetilde{\mathcal{E}} = 0$ at a distance [see Eqs. (4) and (6)]:

$$r_e = r_0 \exp\left(\frac{r_\oplus}{2\,\beta\, r_0}\right) \tag{10}$$

If the mission requirement is to reach a given hyperbolic excess velocity V_∞ with respect to the Sun, the E-sail can be jettisoned when the Sun-spacecraft distance is:

$$r = r_0 \exp\left(\frac{r_\oplus\, V_\infty^2 + \mu_\odot\, r_\oplus/r_0}{2\,\mu_\odot\,\beta}\right) \tag{11}$$

In this case, P_0 is the only trajectory point in which the radial velocity is zero and r_0 is the corresponding perihelion distance.

Case c

The last case is obtained when the energy line intercepts the potential well boundary at three points, P_0, $P_a = (\widetilde{r}_a, \widetilde{\mathcal{E}}_a)$ and $P_b = (\widetilde{r}_b, \widetilde{\mathcal{E}}_b)$, as is shown in Fig. 3. This situation is representative of a low-performance propulsion system, that is, an E-sail with a low characteristic acceleration ($\beta < \beta^\star$). The values of $\widetilde{r}_a$ and $\widetilde{r}_b$, with $0 < r_a < r_t < r_b$, are two of the three real solutions of the nonlinear equation $\widetilde{\mathcal{E}} = \widetilde{\mathcal{E}}_w$, where $\widetilde{\mathcal{E}}$ is given by Eq. (4) and $\widetilde{\mathcal{E}}_w$ by Eq. (5). The nonlinear equation $\widetilde{\mathcal{E}} = \widetilde{\mathcal{E}}_w$ in the unknown $\widetilde{r}$ can be solved numerically, and the solution $\widetilde{r} = 0$ can be discarded as it coincides with r_0. The least of the remaining two solutions corresponds to $\widetilde{r}_a$, that is, the aphelion distance.

The spacecraft motion can be described as follows. Assuming that $\beta \in (0,\, \beta^\star)$, for $t > t_0$ the spacecraft increases its distance from the Sun until, at time t_a, it reaches a distance $r_a < r_t$ (point P_a of Fig. 3). During this phase the spacecraft tracks,

in the energy plane, the segment $\overline{P_0P_a}$. Because P_a belongs to the potential well boundary, at P_a the spacecraft radial velocity is zero, but the radial acceleration is negative. Therefore the spacecraft is subjected to a net inward force, proportional to $\ddot{r}_a$, that curves the trajectory toward the Sun. As a result, the distance from the Sun starts decreasing and the spacecraft tracks backwards the segment $\overline{P_0P_a}$ until it reaches P_0 again (at time t_1). For $t > t_1$ the motion in the energy plane repeats, that is, the spacecraft increases its distance from the Sun until r_a and so on. In other words the spacecraft oscillates indefinitely, in the energy plane, along the segment $\overline{P_0P_a}$. Clearly, the point P_b cannot be reached because the segment $\overline{P_aP_b}$ lies in the forbidden region. Therefore, the value of $\beta^\star$, given by Eq. (9), is the minimum dimensionless characteristic acceleration required to escape from the circular parking orbit of radius r_0. In addition, r_t is the maximum aphelion distance of a closed orbit when the propulsion system is on. When viewed with respect to a heliocentric reference frame, the spacecraft trajectory is constrained within the region between the two circles of radius r_0 (perihelion) and r_a (aphelion). For example Fig. 4 illustrates the spacecraft trajectory for $\beta = 0.9\,\beta^\star \simeq 0.18326896991508\,r_\oplus/r_0$, in which the aphelion distance is $r_a \simeq 2.06\,r_0$.

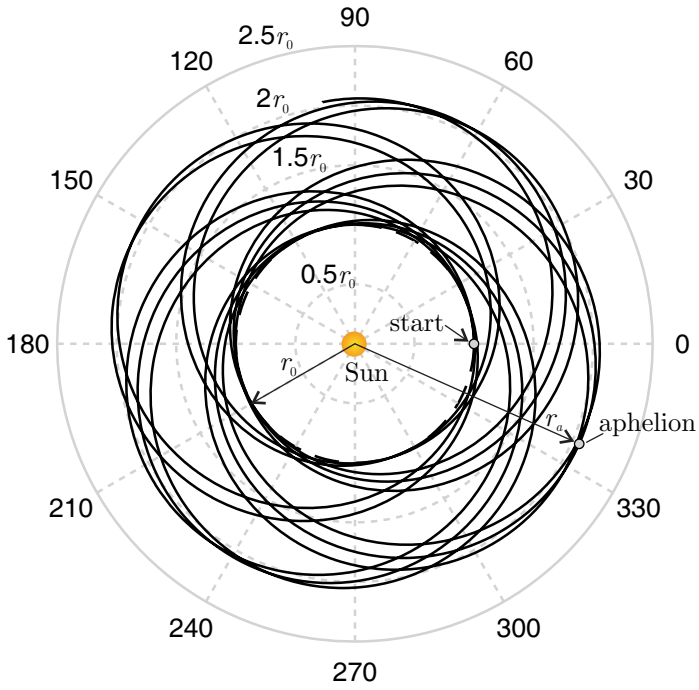

Figure 4: Spacecraft trajectory for $\beta = 0.9\,\beta^\star \simeq 0.18326896991508\,r_\oplus/r_0$ from a circular parking orbit of radius r_0.

3.2 Low-performance E-sail motion with constant cone angle

Analytic trajectories for a spacecraft subjected to a low, continuous, propulsive acceleration are available only for very special cases [8–10]. When a closed-form trajectory corresponding to a given thrust control law cannot be found, a possible option is to introduce suitable simplifications in the differential equations of motion [11–13]. Within this context, it is possible to find an analytical, albeit approximate, expression for the heliocentric trajectory of a spacecraft propelled by a low-performance E-sail. Using a 2D model and under the assumptions of constant thrust angle and low propulsive acceleration modulus, the heliocentric trajectory of a spacecraft start-

ing from a heliocentric circular orbit is obtained in a parametric way as a function of time (details are in Ref. [AD3]).

The propulsive acceleration is modeled by Eq. (1) with $d \triangleq r_\oplus = 1\,\mathrm{au}$, $\eta = 1$ and $a_c \leq 0.1$. Assume now that the cone angle α is maintained constant. Consider an E-sail spacecraft on a heliocentric circular parking orbit, whose position at the initial time instant $t = t_0 \triangleq 0$ is defined by its polar angle θ_0 and distance r_0, see Fig. 2. A good approximation of the spacecraft trajectory is given by [AD3]

$$r = \frac{\mu_\odot}{2\,a_c\,r_\oplus\,\cos\alpha}\,(1-\sqrt{\chi}) \tag{12}$$

$$\theta = \frac{F(\chi_0)-F(\chi)}{2\,\tan\alpha} \tag{13}$$

where

$$\chi \triangleq 1 - \frac{4\,a_c\,r_\oplus\,h^2\,\cos\alpha}{\mu_\odot^2} \tag{14}$$

$$\chi_0 \triangleq \chi(h_0) \tag{15}$$

$$h = h_0 + (a_c\,r_\oplus\,\sin\alpha)\,t \tag{16}$$

where $h_0 = \sqrt{\mu_\odot r_0}$ is the angular momentum along the heliocentric parking orbit and $\mu_\odot$ is the Sun's gravitational parameter.

The expression $r = r(\chi)$ can be used for evaluating the osculating orbit characteristics. In fact, using Eqs. (12)-(16), a closed form approximation of the osculating orbit mechanical energy $\mathcal{E}$ is obtained as

$$\mathcal{E} = \frac{2\,h^2\,a_c^2\,r_\oplus^2\,\sin^2\alpha}{\mu_\odot^2 - 4\,a_c\,r_\oplus\,h^2\,\cos\alpha} + \frac{h^2}{2\,r^2} - \frac{\mu_\odot}{r} \tag{17}$$

Therefore, the semimajor axis a and eccentricity e of the osculating orbit are

$$a = -\mu_\odot/(2\,\mathcal{E}) \tag{18}$$

$$e = \sqrt{1 - 2\,\mathcal{E}\,h^2/\mu_\odot^2} \tag{19}$$

Note that, if $a_c \to 0$, Eq. (17) is exact ($\mathcal{E} = -0.5\,\mu_\odot/r_0$), while if a_c is small, but not zero, the corresponding initial value of $\mathcal{E}$ is slightly overestimated.

The accuracy of the previous analytical results can be compared, by simulation, with a numerical integration of equations of motion using, in both cases, the same parking orbit radius, and the same propulsion system characteristics, that is, a_c and α.

Assuming $r_0 = r_\oplus$, $a_c = 0.1\,\mathrm{mm/s^2}$ and $\alpha = \alpha_{\max}$, the comparison is summarized in Fig. 5 for a ten-years time interval. Figure 5 clearly shows that the analytical approximations of $\mathcal{E}$ and of θ closely follow their numerical counterparts. On the contrary, the numerical simulations of radial distance and eccentricity exhibit an oscillatory behavior superimposed to a secular variation, which is essentially described by Eq. (12). However, the spacecraft trajectory obtained using Eqs. (12) and (13) closely follows the trajectory calculated numerically, as is shown in Fig. 6.

The previous analytical relationships are useful to obtain an estimate of the flight time required by an E-sail to reach a prescribed distance from the Sun. For example, in a hypothetical flyby mission toward Mars ($r = 1.524\,\mathrm{au}$), assuming $a_c = 0.1\,\mathrm{mm/s^2}$ and $\alpha = 30\,\mathrm{deg}$, the flight time obtained integrating the equations of motion is $1603\,\mathrm{days}$, while Eqs. (12)-(16) provide a flight time of $1521\,\mathrm{days}$, with a percentage difference of 5% only with respect to the value obtained by simulation. This difference is further reduced in a flyby mission to Venus ($r = 0.723\,\mathrm{au}$, $a_c = 0.1\,\mathrm{mm/s^2}$ and $\alpha = -30\,\mathrm{deg}$) in which the mission time is $1061\,\mathrm{days}$ (numerical simulation), while the analytic model estimates $1063\,\mathrm{days}$.

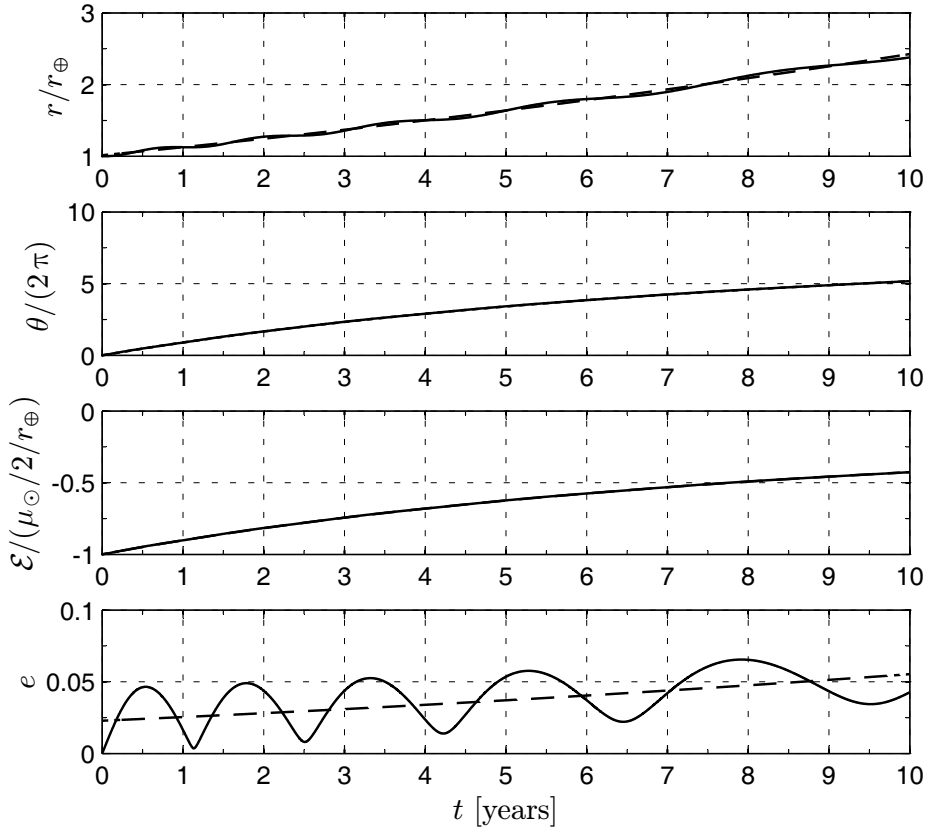

Figure 5: Simulation results for a ten-years orbit raising with $a_c = 0.1$ mm/s^2, $\alpha = 30\,\mathrm{deg}$, and $r_0 = r_\oplus$ (solid line = numerical; dashed line = approximated).

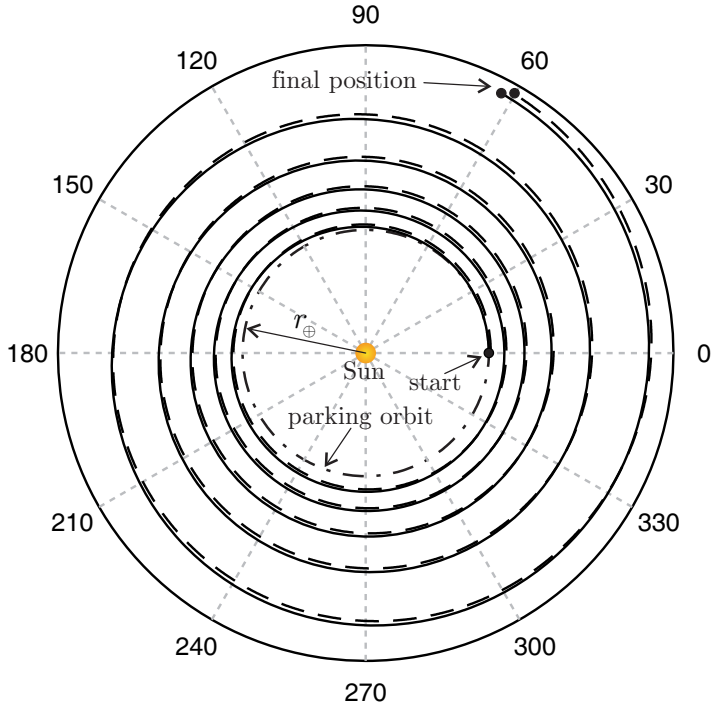

Figure 6: Spacecraft trajectory in a ten years orbit raising ($a_c = 0.1$ mm/s^2, $\alpha = 30\,\mathrm{deg}$, and $r_0 = r_\oplus$).

4 Outer Solar System missions

Sending a spacecraft to the outer Solar System (SS) boundaries is widely considered as the primary means to obtain a more comprehensive knowledge of the heliosphere and the nearby interstellar medium. E-sails offer an interesting option for missions toward the boundaries of the Solar System, in which long transfer times are in general required. In this section we investigate the performance of an E-sail propulsion system required for obtaining escape conditions from the SS and for planning a mission to reach the heliosphere boundaries.

The study of the problem can be addressed in an optimal framework by looking for the minimum time (t_2) necessary to reach a given solar distance (r_2) or a given hyperbolic excess speed (V_∞) using a 2D framework (for further details, see Ref. [AD4]). Such information can then be employed as a starting point for a more accurate Three-Dimensional (3D) analysis.

The results obtained for the 2D analysis are based on the study of trajectories in a heliocentric polar reference frame $\mathcal{T}_\odot(r,\theta)$. At the initial time t_0 the E-sail is placed, at a distance r_0 from the Sun, on a heliocentric elliptic orbit with given values of semimajor axis a and eccentricity e, see Fig. 2. The E-sail propulsive acceleration is modeled on the basis of Eq. (1) with $d = 1\,\mathrm{au}$ (a_c is now referred to as $a_\oplus$), $\eta = 7/6$, and $\alpha_{\max} = 35\,\mathrm{deg}$.

Simulations have shown that a generic optimal trajectory may include a close approach to the Sun for increasing the spacecraft propulsive acceleration. Indeed, it is possible that, in an initial phase, the spacecraft goes toward the Sun to exploit the increased available thrust resulting from the growing solar wind electron density and temperature [1, 4, 5]. Such a behavior is usually referred to as Solar Wind Assist (SWA) and is frequently used in solar sail based missions [14, 15]. However, when a mission includes a SWA, the Sun-spacecraft distance cannot decrease below a minimum admissible value $r_{\min}$ imposed by thermal and mechanical constraints involving the E-sail tethers, see Fig. 2. Preliminary estimates suggest assuming $r_{\min} = 0.5\,\mathrm{au}$ when aluminium tethers are used, while copper tethers are expected to guarantee a further reduction in the minimum distance up to $r_{\min} = 0.33\,\mathrm{au}$. The case of a trajectory in which the E-sail increases, at any time, its instantaneous spacecraft distance from the Sun will be referred to as Direct Transfer (DT).

4.1 Minimum time to achieve escape conditions

Consider first the problem of generating trajectories that allow an E-sail to escape from the SS, that is, with zero hyperbolic excess energy with respect to the Sun ($V_\infty = 0$).

Assuming a circular starting orbit ($e = 0$ and $a = 1\,\mathrm{au}$), t_2 is independent of the spacecraft initial position. The mission times t_2 obtained from simulations as a function of the characteristic acceleration are shown in Fig. 7.

The escape time is usually tolerable, being less than $4.6\,\mathrm{years}$, even for moderate values of the characteristic acceleration. However, depending on $a_\oplus$ the optimal escape condition are achieved with different type of trajectories. In fact, if $a_\oplus$ is less than $0.55\,\mathrm{mm/s^2}$, the spacecraft tracks a SWA trajectory without activating the constraint on $r_{\min} = 0.5\,\mathrm{au}$. When the value of the characteristic acceleration ranges in the interval $[0.54, 1.16]\,\mathrm{mm/s^2}$, the spacecraft goes very close to the Sun up to the minimum admissible distance $r_{\min}$. On the other hand, when $a_\oplus > 1.16\,\mathrm{mm/s^2}$ the optimal escape condition is obtained using a DT trajectory.

The spacecraft behavior is better understood with the aid of Fig. 8, which illustrates the spacecraft trajectory for three different values of characteristic acceleration.

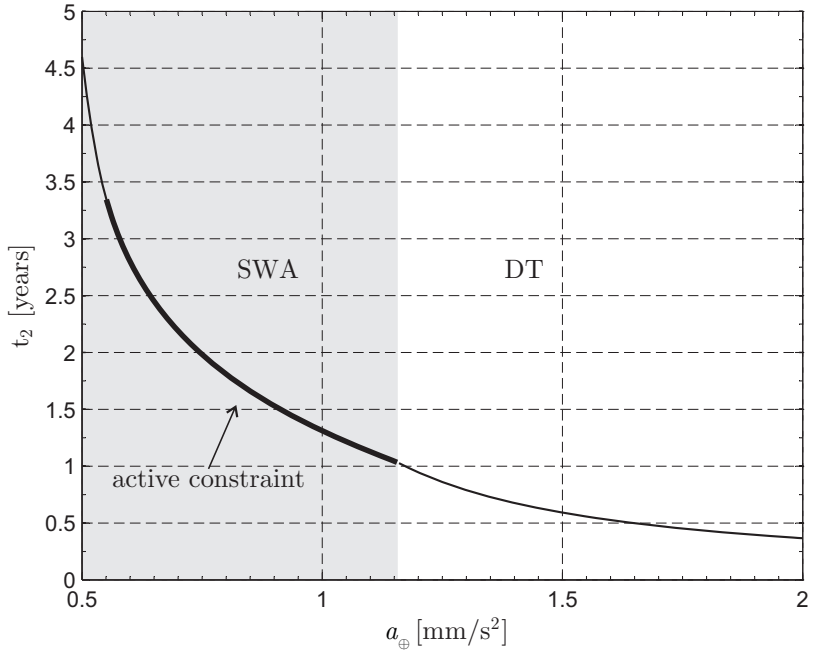

Figure 7: Minimum escape times from Earth circular orbit ($r_{\min} = 0.5\,\mathrm{au}$).

In particular, the three typologies correspond to a SWA trajectory with inactive constraint ($a_\oplus = 0.5\,\mathrm{mm/s^2}$), a SWA trajectory with active constraint ($a_\oplus = 1\,\mathrm{mm/s^2}$) and a DT trajectory ($a_\oplus = 1.5\,\mathrm{mm/s^2}$). Note that coasting phases ($\tau = 0$, the E-sail thrust is switched off) exist in SWA trajectories. Figure 9 compares the sail cone angle $\alpha(t)$ for the three cases with $a_\oplus \in \{0.5,\, 1,\, 1.5\}\,\mathrm{mm/s^2}$. While in a DT angle α is constant and equal to $\alpha_{\max}$ during the whole mission, in a SWA trajectory the cone angle experiences a sign variation during the perihelion approaching phase ($t \in [t_0,\, t_1]$).

Figure 10 shows the sensitivity of the escape time and escape distance $r(t_2)$ with respect to the value of $r_{\min}$. The flight times have been normalized by the escape times corresponding to $r_{\min} = 0.5\,\mathrm{au}$, and taken from Fig. 7. The analysis is confined to the range $a_\oplus \in [0.55,\, 1]\,\mathrm{mm/s^2}$, within which from the previous discussion the constraints $r_{\min} = 0.5\,\mathrm{au}$ would be activated. Figure 10 shows that the performance improvements obtained by decreasing $r_{\min}$ are moderate.

When the initial orbit coincides with the actual heliocentric orbit of Earth, that is, $a = 1\,\mathrm{au}$ and $e = 0.01671123$, the polar symmetry is lost, and the mission performance must be studied by varying the initial true anomaly in the range $\theta_0 \in [0,\, 2\,\pi]$. In this case the transition between SWA and DT strategies is essentially independent of θ_0 and is obtained when $a_\oplus \simeq 1.2\,\mathrm{mm/s^2}$. Moreover, the initial orbit eccentricity has a negligible effect on t_2 when $a_\oplus$ ranges in the interval $[0.5,\, 2]\,\mathrm{mm/s^2}$.

In conclusion, results taken from Fig. 7 are a good approximation of the minimum time to achieve escape conditions from SS. Note that, once the escape condition is met, the spacecraft is on a parabolic orbit, and the E-sail propulsion system could be jettisoned in such a way that the payload alone can continue its travel toward the deep space with a flight by inertia.

4.2 Minimum time to achieve a given solar distance

Assume now that the mission aim is to reach a given solar distance $r_2 \in [5,\, 100]\,\mathrm{au}$ in the least amount of time with medium-high performance E-sails ($a_\oplus \in [1,\, 2]\,\mathrm{mm/s^2}$).

A preliminary analysis of this problem confirms that the Earth’s orbital eccentricity

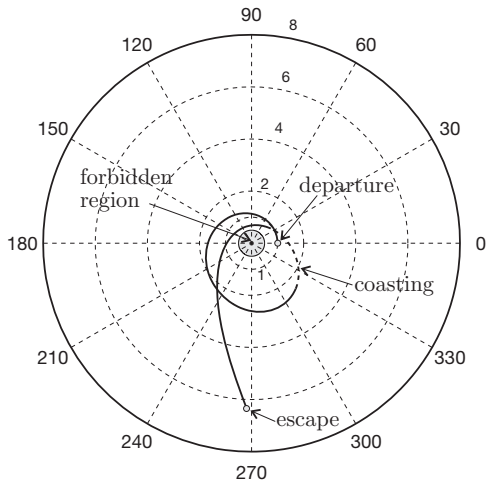

(a) SWA with inactive constraint ($a_\oplus = 0.5\,\mathrm{mm/s^2}$, $t_2 \simeq 4.6\,\mathrm{years}$).

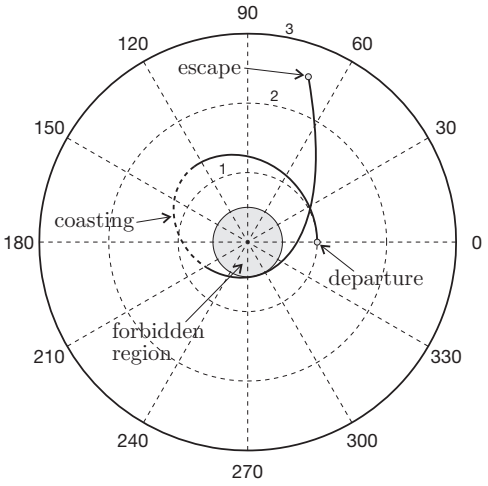

(b) SWA with active constraint ($a_\oplus = 1\,\mathrm{mm/s^2}$, $t_2 \simeq 1.31\,\mathrm{years}$).

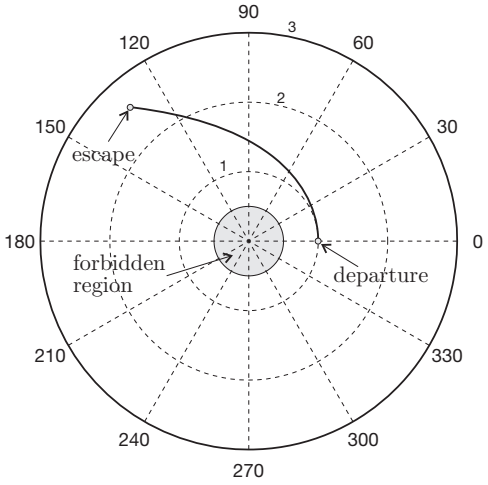

(c) DT ($a_\oplus = 1.5\,\mathrm{mm/s^2}$, $t_2 \simeq 0.59\,\mathrm{years}$).

Figure 8: Escape trajectories from a circular orbit ($r_{\min} = 0.5\,\mathrm{au}$).

has a negligible effect on the mission performance. Therefore, the initial parking orbit is assumed to be circular with a radius equal to $1\,\mathrm{au}$.

The solutions of the optimal problem are summarized in Fig. 11. The DT strategy is superior to the SWA in the gray region highlighted in Fig. 11. This region is confined to somewhat small values of r_2 when compared to the characteristic dimensions of the SS and to the heliosheath distance (roughly $100\,\mathrm{au}$). Therefore, missions toward the outer SS require a SWA strategy unless very high performance E-sails are considered (that is, $a_\oplus > 4\,\mathrm{mm/s^2}$).

Simulations show that in all the analyzed cases the specific mechanical energy at r_2 is positive. This means that the spacecraft at the end of its nominal trajectory is on a hyperbolic orbit with hyperbolic excess speed V_∞, see Fig. 12. Note that V_∞ takes high values especially when substantial characteristic accelerations are used. For example, assuming $a_\oplus = 2\,\mathrm{mm/s^2}$, the hyperbolic excess speed at the end of a mission toward the heliosheath ($r_2 \simeq 100\,\mathrm{au}$) is $V_\infty \simeq 10\,\mathrm{au/year}$. This hyperbolic excess speed is sufficiently high to jettison the E-sail and allow the spacecraft to extend the original mission and continue its travel with a cruise speed roughly coincident with

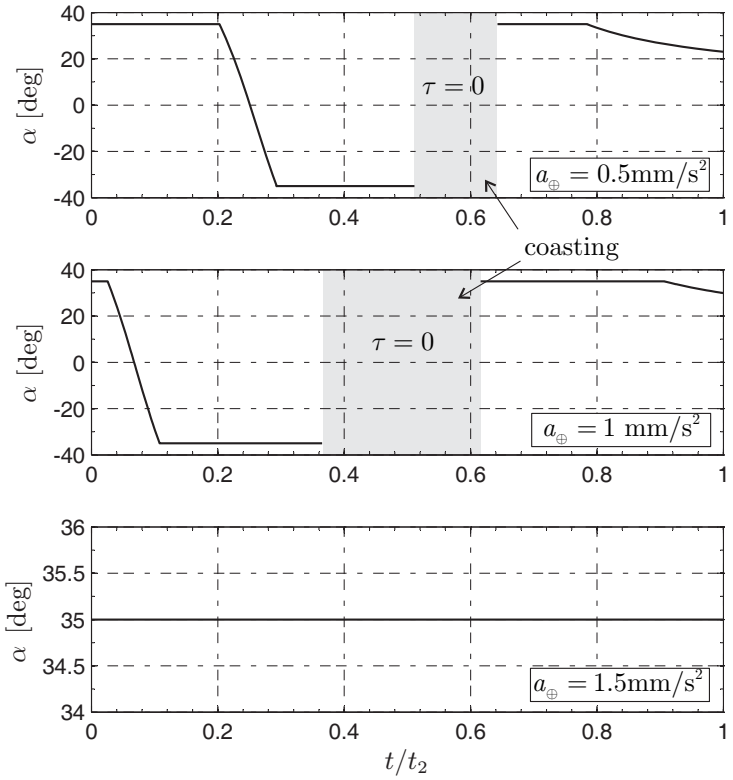

Figure 9: Sail cone angle for minimum-time escape trajectories from a circular orbit of radius $1\,\text{au}$ ($r_{\min} = 0.5\,\text{au}$).

V_∞.[1]

Simulations show, that the perihelion constraint (when $r_{\min} \in [0.3,\, 0.5]\,\text{au}$) does not significantly affect the mission performance, see Fig. 13. Figure 13 also shows that, in general, the heliosheath nose may be reached[2] in about $15\,\text{years}$ with a medium-performance E-sail, having a characteristic acceleration of $1.15{-}1.25\,\text{mm/s}^2$.

Finally, trajectory simulations show that, in analogy to the escape trajectories from the SS, missions toward the heliosheath are characterized by the constraint activation on the minimum distance from the Sun and by a single coasting phase.

4.3 Optimal 3D trajectories toward the heliosheath

Both the heliosphere and the heliosheath are shaped by the interaction of the solar wind with the local interstellar medium [16], and, currently, the ecliptic latitude and longitude of the heliosheath nose are given by $\phi_H = 7.5\,\text{deg}$ and $\psi_H = 254.5\,\text{deg}$, respectively. This means that missions toward the heliosheath nose require to be studied in a 3D framework.

To deal with the 3D case, a suitable heliocentric spherical reference system $\mathcal{T}_\odot(r, \psi, \phi)$ is introduced, where ψ is the ecliptic longitude and ϕ is the ecliptic latitude. In such a reference frame, minimum time trajectories toward the heliosheath nose can be studied assuming an initial circular orbit with radius equal to $1\,\text{au}$, a minimum distance $r_{\min} = 0.5\,\text{au}$, a characteristic acceleration ranging in the interval $a_\oplus \in [1,\, 2]\,\text{mm/s}^2$, and using the fact that the constraint on the minimum distance is active.

[1] To make a comparison with current missions, Voyager 1 is escaping from the SS at a speed of about $3.6\,\text{au/year}$, while Voyager 2 is escaping at a speed of $3.3\,\text{au/year}$.

[2] As a comparative example, Voyager 1 reached a solar distance of $100\,\text{au}$ $29\,\text{years}$ after its departure.

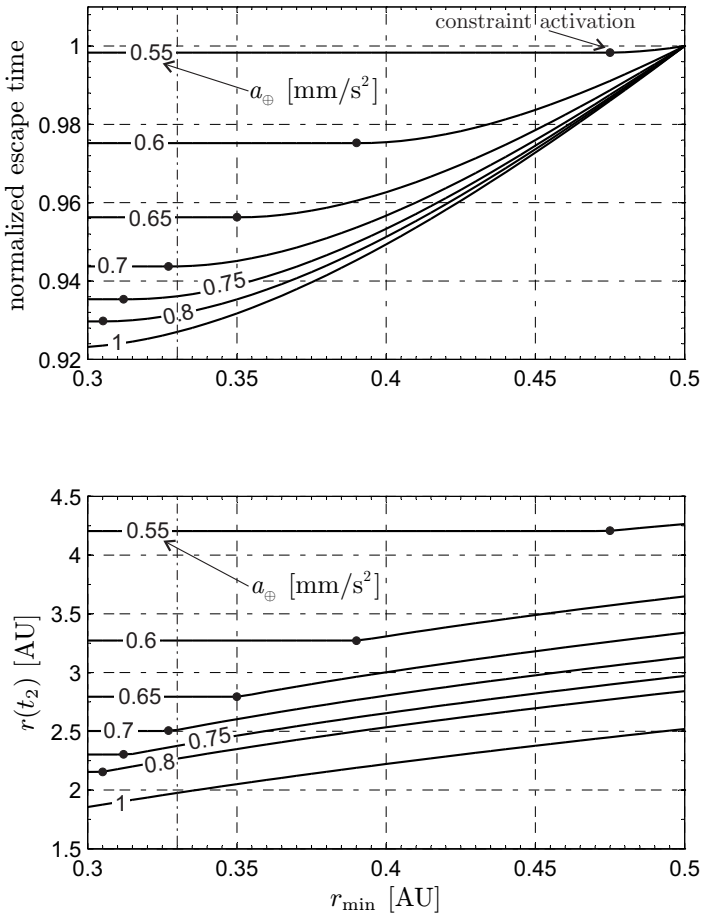

Figure 10: Escape time from Earth circular orbit and escape distance as a function of $a_\oplus$ and $r_{\min}$.

The variation of t_2 with $a_\oplus$ is illustrated in Fig. 14(a) where the flight time corresponding to the 2D case is displayed for comparison. Figure 14(a) shows the increase of t_2 in the transition from the 2D to the 3D case. Such a behavior may be explained by observing that the required variation of the orbital plane takes place during the approaching phase to the Sun and soon after the SWA, when the propulsive acceleration attains its maximum value. Unlike the 2D case, the propulsive acceleration is used, in part, to vary the value of ϕ instead of increasing the spacecraft specific mechanical energy. This reduced capability of exploiting the SWA in a 3D trajectory increases with a decrease of $a_\oplus$, and is ultimately responsible of the differences in mission times between the two models. However, such an increase tends to reduce with an increase of the characteristic acceleration. For example, when $a_\oplus = 2\,\mathrm{mm/s^2}$, the difference in flight time for the two models is only 5 months, that is, less than 3.5% of the total mission time.

Figure 14(b) shows the variation in initial spacecraft longitude ψ_0 with $a_\oplus$. This happens because the starting spacecraft longitude $\psi_0 \triangleq \psi(t_0)$ is an unknown of the problem since, contrary to the planar case, in a 3D space the cylindrical symmetry of the problem is lost. Moreover, the information on the value of ψ_0 is useful for estimating the spacecraft launch window. Note that, because the position of the heliosheath nose is nearly independent of time, the launch window obtainable from Fig. 14(b) repeats every year.

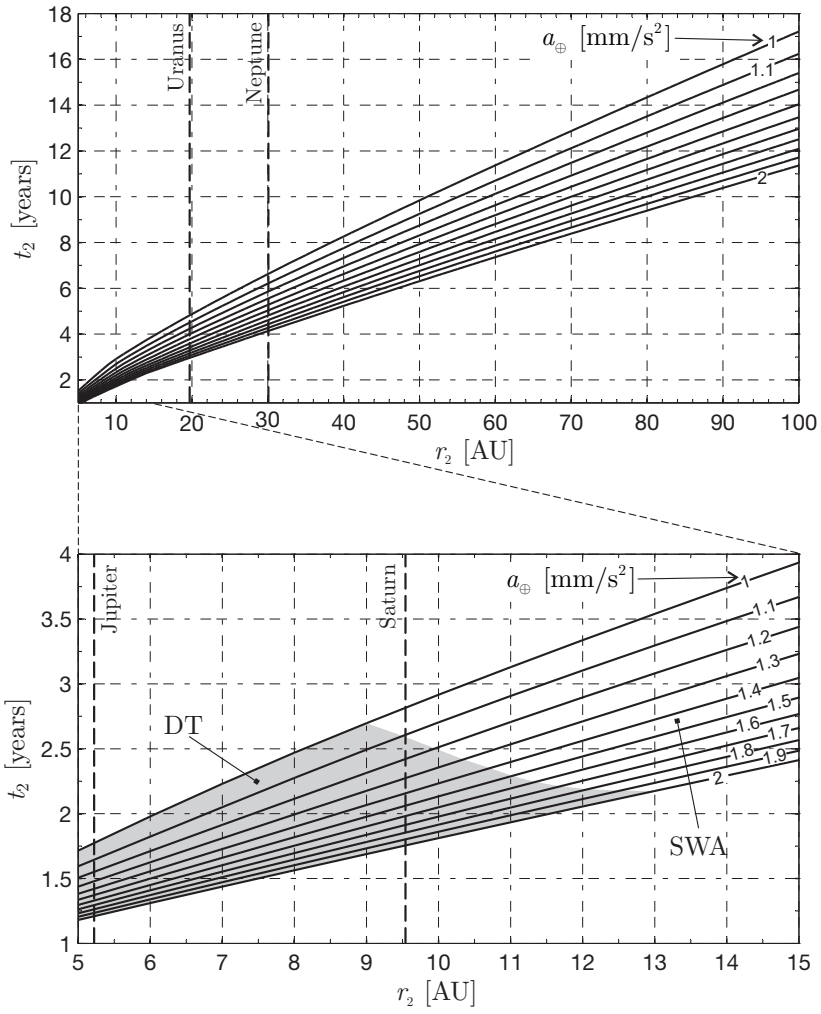

Figure 11: Minimum flight time t_2 vs. final solar distance r_2 ($r_{\min} = 0.5\,\mathrm{au}$).

4.3.1 Near-Optimal trajectories

Because the modulus of the propulsive acceleration decreases sharply with the Sun's distance, it is possible to imagine an alternative mission strategy in which the E-sail is jettisoned at a distance $r_c < r_2$ where the propulsive acceleration can be considered negligible with respect the initial value (for example $a_p/a_\oplus \simeq 6.8\%$ if $r_c = 10\,\mathrm{au}$).

Such a strategy, similar to what was studied by Sauer in Ref. [17] for solar sails, plans a flight by inertia between r_c and r_2, thus simplifying the acquisition of science data without any interference with the sail and reducing the requested lifetime of the sail. Using such a mission strategy, several new trajectories toward the heliosheath nose have been simulated. In accordance to Sauer [17], and to obtain a direct comparison with solar sails-based scenarios, a cutoff distance of $r_c = 5\,\mathrm{au}$ was enforced in the simulations. Also, only solutions with flight times less than $20\,\mathrm{years}$ have been considered. The simulation results, using three possible values of minimum solar distance $r_{\min} = (0.33,\, 0.4,\, 0.5)\,\mathrm{au}$, are summarized in Fig. 15.

In comparison with the results from Ref. [17], it should be noted that, the minimum perihelion distance being equal ($r_{\min} = 0.4\,\mathrm{au}$), the E-sail and the solar sail present similar performance for $a_\oplus \simeq 2\,\mathrm{mm/s^2}$, whereas for smaller values of characteristic acceleration a solar sail is definitely superior to an E-sail. The reason is that a solar sail has a more pronounced thrust increase with respect to an E-sail in the nearness

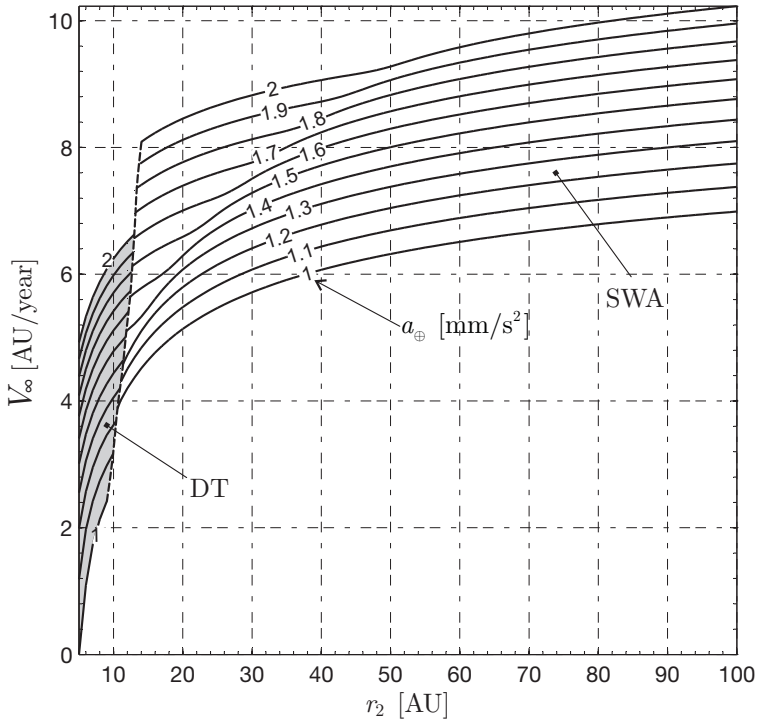

Figure 12: Hyperbolic excess speed V_∞ as a function of the final solar distance r_2 ($r_{\min} = 0.5\,\mathrm{au}$).

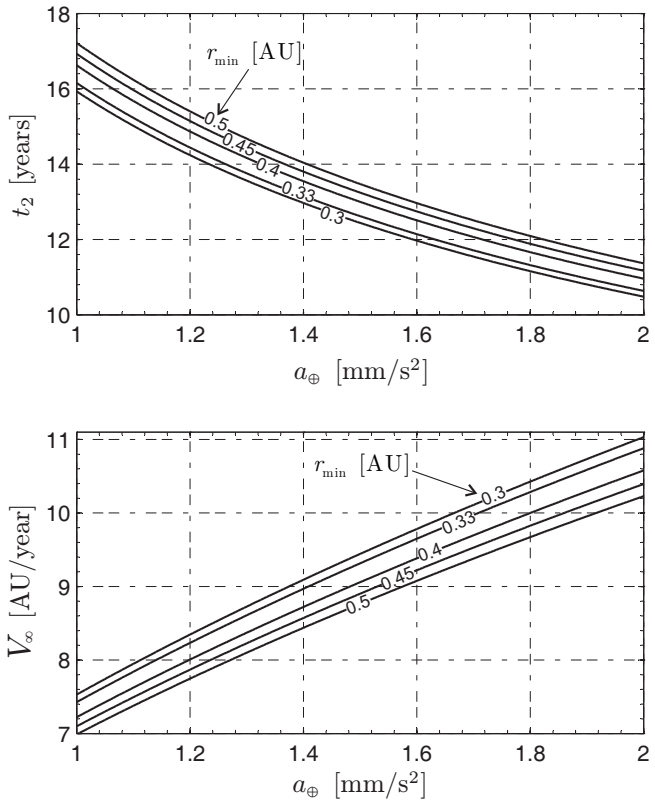

Figure 13: Optimal performance for missions toward the heliosheath ($r_2 = 100\,\mathrm{au}$).

of the perihelion. On the other hand an E-sail produces a higher thrust for distances $r > r_\oplus$, but such an advantage is reduced by the constraint on r_c.

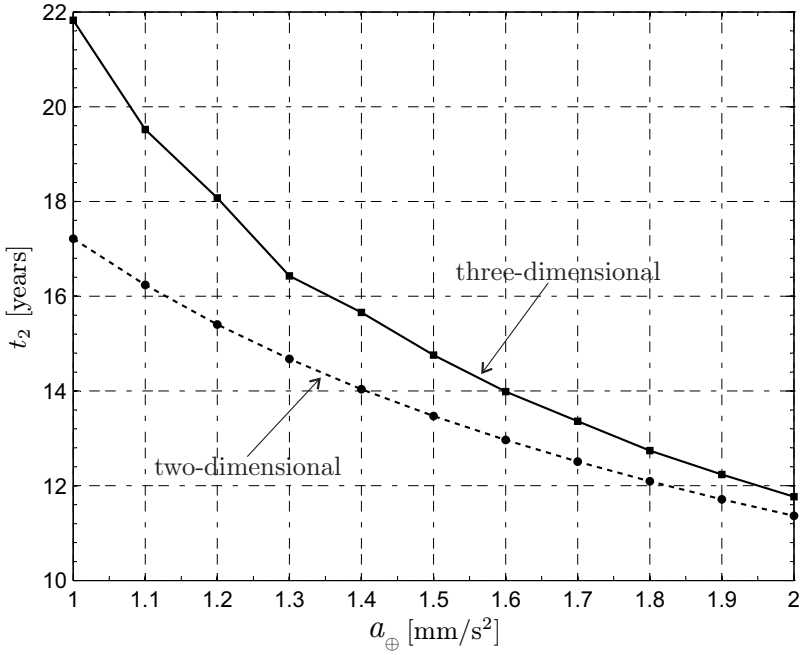

(a) Flight time.

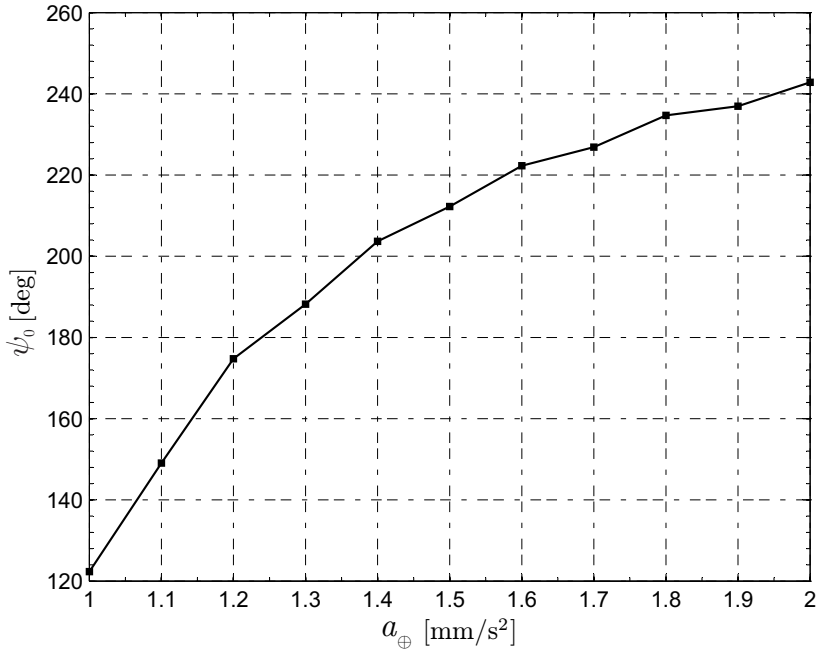

(b) Initial heliocentric longitude.

Figure 14: Mission performance toward the heliosheath nose ($r_2 = 100\,\mathrm{au}$) with $r_{\min} = 0.5\,\mathrm{au}$.

It is possible to investigate the influence of r_c on the mission time t_2. Assuming $r_{\min} = 0.5\,\mathrm{au}$ and varying the cutoff distance in the range $r_c \in [5,\, 30]\,\mathrm{au}$, which corresponds to jettison the sail at a Sun's distance between Jupiter and Neptune, the results obtained are shown in Fig. 16. As expected, increasing the cutoff distance and the characteristic acceleration, the mission time t_2 is reduced. Note that when the sail is jettisoned at a distance greater than $15\,\mathrm{au}$, it is possible to reach the heliosheath nose in less than $20\,\mathrm{years}$ using characteristic accelerations that do not exceed $1.2\,\mathrm{mm/s^2}$.

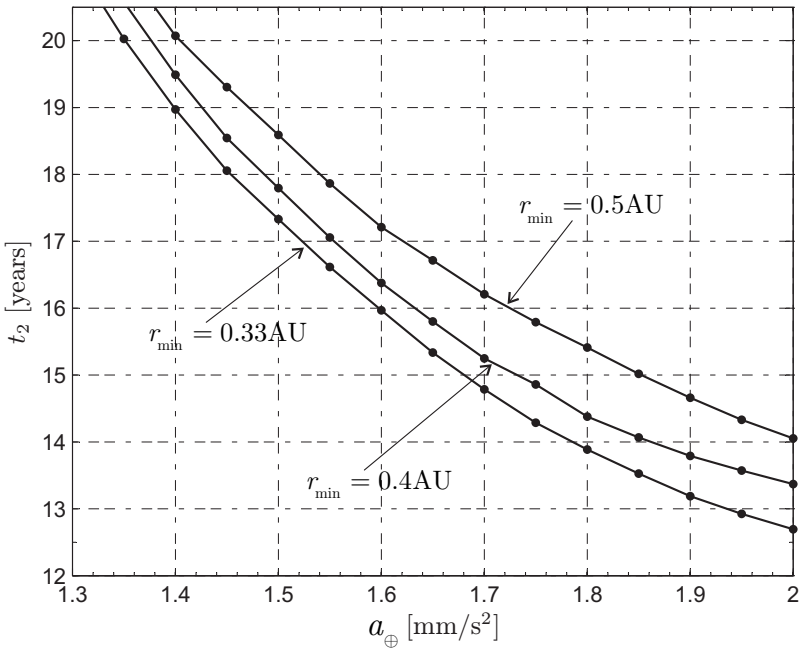

Figure 15: Flight time for missions toward heliosheath nose ($r_2 = 100\,\text{au}$) with $r_c = 5\,\text{au}$.

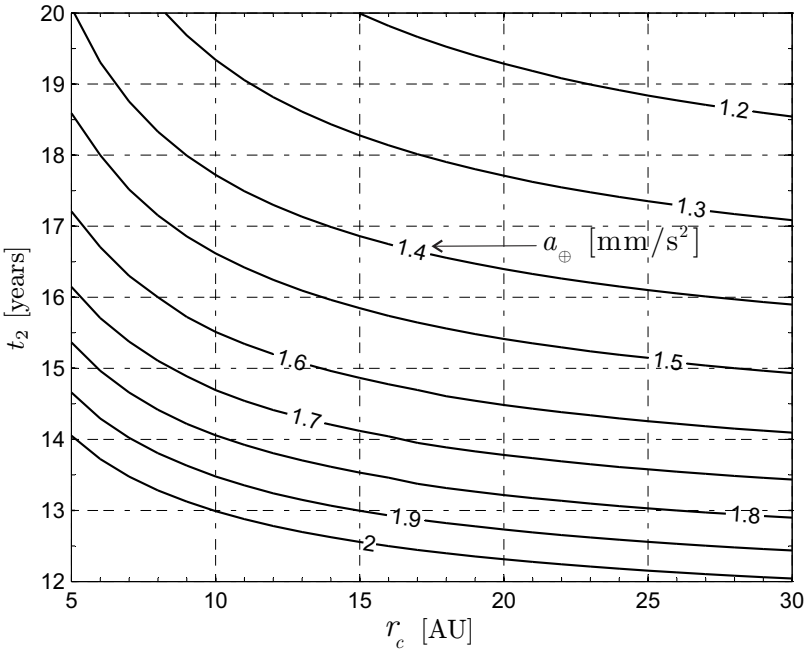

Figure 16: Flight time for missions toward heliosheath nose ($r_2 = 100\,\text{au}$) as a function of r_c ($r_{\min} = 0.5\,\text{au}$).

Clearly, as r_c is increased, the sail operating time length $t_c \triangleq t(r = r_c)$ increases as well. By simulations, it is found that if $r_c < 30\,\text{au}$ and $a_\oplus > 1.2\,\text{mm/s}^2$ the operating time t_c is less than $6\,\text{years}$, that is, it is much less than the propulsion system lifetime of $10\,\text{years}$ conjectured in Ref. [18]. The hyperbolic excess speed V_∞ varies, in its turn, with r_c, and is less than $10\,\text{au/years}$ in all the simulations.

4.4 E-sail for Interstellar Heliopause Probe

The Interstellar Heliopause Probe (IHP) primary scientific aim [16] is that of analyzing the heliopause and the interstellar medium through in situ measurements with a highly miniaturized and a highly integrated payload suite [19]. Preliminary studies [16, 20] have estimated that the payload suite, with a mass of about $20\,\mathrm{kg}$, can be accommodated inside a small spacecraft (the spacecraft platform) having an overall mass of $m_p = 213\,\mathrm{kg}$. Such a platform, equipped with a suitable propulsion system, should be able to reach the heliopause ($r_2 = 200\,\mathrm{au}$) within $25\,\mathrm{years}$ of transfer time [20]. Among the primary propulsion systems examined so far, solar sails were the only solution capable of meeting all the mission requirements [19], especially as far as the total mission time is concerned. In addition, the current conception of IHP mission requires that the primary propulsion system (that is, the solar sail) is jettisoned at a solar distance of $5\,\mathrm{au}$. As discussed above, this choice simplifies the scientific measurements avoiding any interference with the sail and, at the same time, reduces the propulsion system operating time, thus reducing the mission failure probability [17]. However simulations have shown that, unlike the solar sail option, an E-sail jettison at a distance of $5\,\mathrm{au}$ is unfeasible unless it is possible to tolerate either much higher values of characteristic acceleration or much higher transfer times.

Using three reasonable values of characteristic acceleration (see [AD4]), that is, $a_\oplus \in \{1.8,\, 1.9,\, 2\}\,\mathrm{mm/s^2}$ and corresponding cutoff distance $r_c \in \{26,\, 15,\, 10\}\,\mathrm{au}$ providing mission transfer time within $25\,\mathrm{years}$, the minimum time trajectory toward the heliopause nose ($r_2 = 200\,\mathrm{au}$, $\psi(t_2) = \psi_H$, and $\phi(t_2) = \phi_H$) has been found by solving an optimal control problem. The results corresponding to the three simulations have been summarized in Table 1.

$a_\oplus$ [mm/s^2]	r_c [AU]	ψ_0 [deg]	t_1 [yrs]	t_c [yrs]	t_2 [yrs]	t_{on} [yrs]	V_∞ [AU/yr]
1.8	26	189.4	0.935	4.19	24.99	3.69	8.31
1.9	15	190	1.034	2.87	24.97	2.28	8.32
2.0	10	190.2	1.157	2.34	24.9	1.66	8.36

Table 1: Mission toward the heliopause nose ($r_2 = 200\,\mathrm{au}$) with $r_{\min} = 0.5\,\mathrm{au}$.

All the three cases give the same launch window (ecliptic longitude $\psi_0 \simeq 190\,\mathrm{deg}$) and provide nearly the same value of hyperbolic excess speed $V_\infty \simeq 8.3\,\mathrm{au/year}$. From Table 1, the time t_{on} during which the E-sail operates is, in the worst case with $a_\oplus = 1.8\,\mathrm{mm/s^2}$, slightly superior to 3.5 years. By comparing the value of t_{on} with that of t_c, it can be deduced that in the interval $t \in [t_0,\, t_c]$ the optimal trajectory displays at least one coasting phase.

The coasting phase and the time history of the state variables are shown in Fig. 17, which illustrates the simulation results corresponding to $a_\oplus = 2\,\mathrm{mm/s^2}$ for $2.5\,\mathrm{years}$ from the departure. The three-dimensional trajectory and its projection on the ecliptic plane are shown in Fig. 18. The time history of the three control variables (τ, α, and δ) are summarized in Fig. 19 in which the sail jettison distance ($r_c = 10\,\mathrm{au}$) and the spacecraft initial angular position $\psi_0 \simeq 190\,\mathrm{deg}$ are both highlighted.

A simplified mass budget analysis (see [AD4]) reveals that the IHP spacecraft launch mass with E-sail option is between $750\,\mathrm{kg}$ and $834\,\mathrm{kg}$ (considering safety margin of 20%). This value is much less than the launch mass capability of the launch vehicle Soyouz-Fregat 2-1B conjectured for a mission scenario with a solar sail [16].

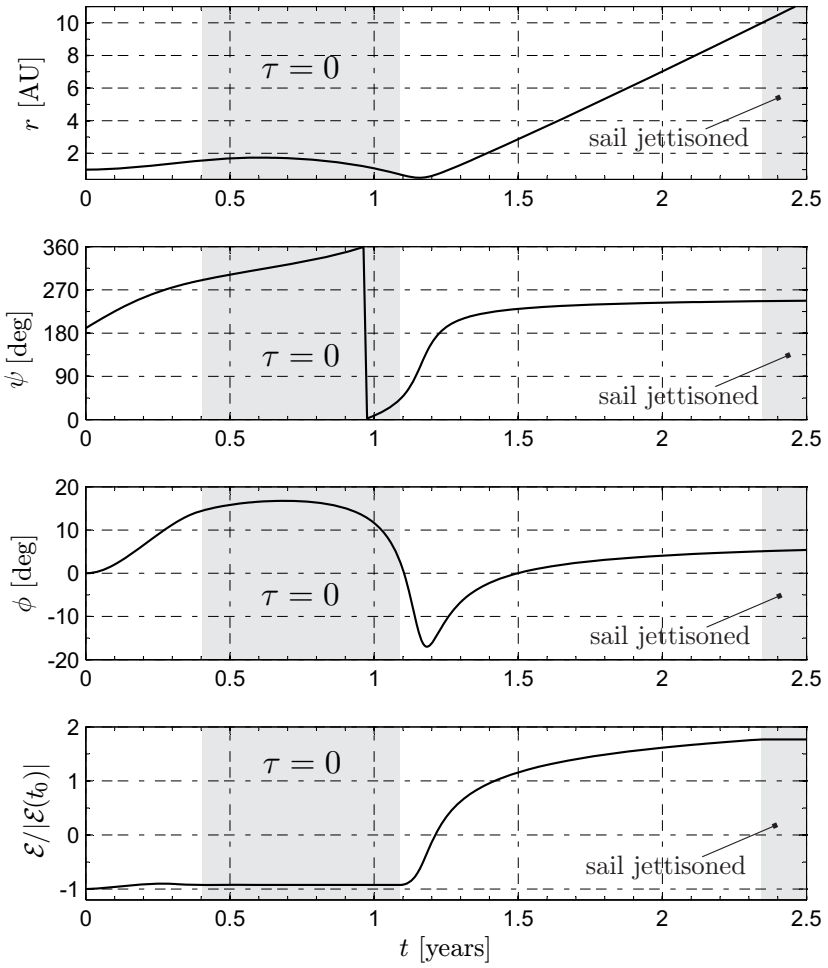

Figure 17: State parameters time histories for a mission toward the heliopause nose ($r_{\min} = 0.5\,\mathrm{au}$)

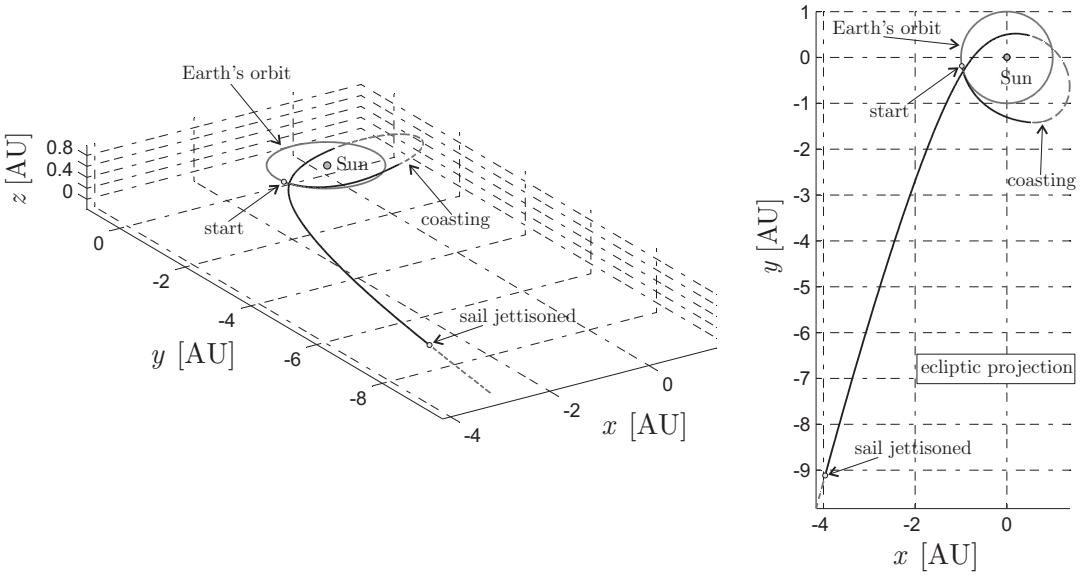

Figure 18: First part of the transfer trajectory toward the heliopause nose ($r_{\min} = 0.5\,\mathrm{au}$).

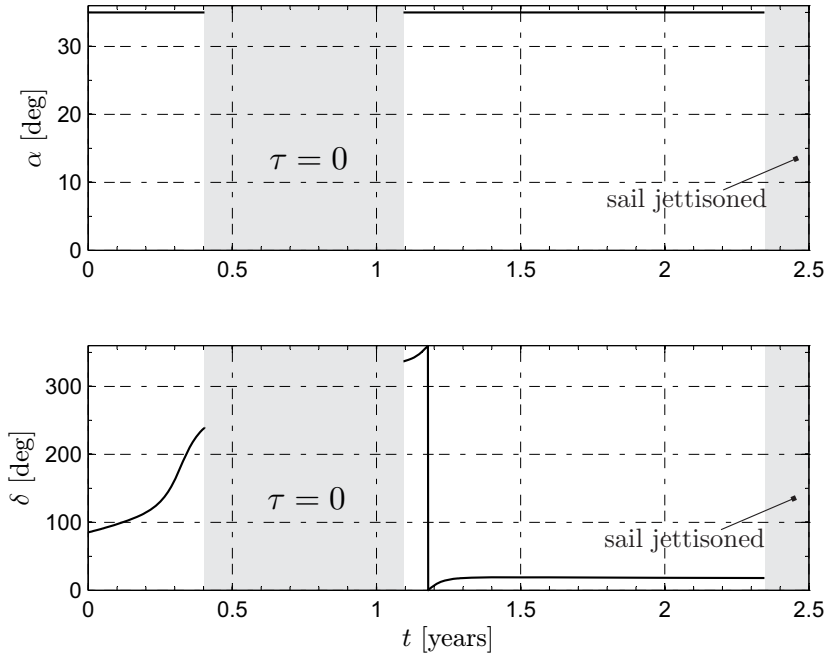

Figure 19: Controls time histories for a mission toward the heliopause nose ($r_{\min} = 0.5\,\mathrm{au}$).

5 Interplanetary missions

E-sails offer an interesting option for interplanetary mission transfers especially if they are coupled with a high-thrust propulsion system. Such a combination represents a useful alternative for reducing the large amount of propellant mass required by conventional chemical thruster and for avoiding complex trajectories with gravity assist maneuvers. Because an E-sail cannot operate inside the planetary magnetosphere, an interplanetary mission strategy is likely to use the additional high-thrust propulsion systems for the escape and/or capture phases, whereas the E-sail provides the thrust for the heliocentric transfer. This may be referred to as a hybrid configuration [21,22], and is actually the starting point of the following analysis.

The hybrid propulsion concept has been employed within a 2D transfer toward a planet of the Solar System, assuming coplanar and circular heliocentric orbits for both the Earth and the target planet. The problem has been studied using a heliocentric polar inertial frame $\mathcal{T}_\odot(r,\,\theta)$, see Fig. 2 and Ref. [AD5] for further details.

The spacecraft starts its mission from the circular orbit of the Earth (that is, $r(t_0 = 0) = r_\oplus = 1\,\mathrm{au}$), and, after the heliocentric transfer, it reaches the planet's orbit (that is, $r(t_f) = r_o$) with some hyperbolic excess velocity V_∞ relative to the planet. The amount of final hyperbolic excess velocity is tolerated in order to decrease the mission flight time, and is used as a simulation parameter for a tradeoff study in which the minimum flight time is related to the total velocity variation required by the chemical thruster to accomplish the mission, that is, for Earth escape and planetary capture.

Each transfer mission has been investigated in a parametric way for different values of characteristic acceleration and hyperbolic excess velocity with respect to the target planet. The obtained results have been arranged in graphs in which the hyperbolic excess velocity V_∞ and the flight time t_f are made dimensionless by dividing their values by the velocity variation ΔV_H and mission time t_H corresponding to a Hohmann heliocentric transfer. These reference values are summarized in Table 2.

Planet	r_p [AU]	ΔV_H [km/s]	t_H [years]
Mercury	0.387	17.144	0.289
Venus	0.723	5.202	0.399
Mars	1.524	5.593	0.708
Jupiter	5.203	14.436	2.731
Saturn	9.537	15.731	6.046
Uranus	19.191	15.940	16.039
Neptune	30.069	15.707	30.613

Table 2: Earth-Planet Hohmann transfer performance.

The E-sail propulsive acceleration is modeled using Eq. (1) with $d = 1\,\mathrm{au}$ ($a_c \equiv a_\oplus$), $\eta = 7/6$, and $\alpha_{\max} = 35\,\mathrm{deg}$.

5.1 Missions toward inner planets

Earth-Mercury trajectories have been studied by varying the characteristic acceleration in the range $a_\oplus \in [1,\, 2]\,\mathrm{mm/s^2}$ and the hyperbolic excess velocity in the range $V_\infty \in [0,\, 0.5]\,\Delta V_H \simeq [0,\, 8.6]\,\mathrm{km/s}$. Note that the results based on a circular coplanar heliocentric orbit of Mercury are not accurate. In fact Mercury has the largest orbital inclination (about $7\,\mathrm{deg}$) and eccentricity (about 0.205) of all planets. A maneuver involving an inclination variation of $7\,\mathrm{deg}$ costs at least $3.6\,\mathrm{km/s}$ in terms of ΔV, and even more for an E-sail mission in which the inclination change cannot be impulsive. Also note that Mercury is very close to the Sun and both thermal and mechanical stresses of the tethers must be considered during the mission planning. The simulation results are shown in Fig. 20(a). A rendezvous mission toward Mercury with an E-sail of mean performance ($a_\oplus = 1\,\mathrm{mm/s^2}$) requires a minimum flight time of 9 months. Although, an increase in V_∞ corresponds to a flight time decrease, such a reduction is not marked. For example, assuming $V_\infty = 0.5\,\Delta V_H \simeq 8.57\,\mathrm{km/s}$, the flight time is 7.17 months, with a reduction of only 20% with respect to the rendezvous case ($V_\infty = 0$).

The simulations for Earth-Venus missions, calculated with $a_\oplus \in [0.5,\, 2]\,\mathrm{mm/s^2}$ and $V_\infty \in [0,\, 1]\,\Delta V_H \simeq [0,\, 5.2]\,\mathrm{km/s}$, are summarized in Fig. 20(b). In this case, due to the small eccentricity of Venus' orbit ($e \simeq 6.77 \times 10^{-3}$), the results for circular orbits are much more representative of a realistic transfer. A rendezvous mission with a spacecraft having $a_\oplus = 1\,\mathrm{mm/s^2}$ requires 6.8 months only. Note that halving the characteristic acceleration, the flight time increase does not exceed 22%. Accordingly, an increase in the hyperbolic excess velocity at arrival does not provide a substantial advantage in terms of flight time.

The results for Earth-Mars missions, calculated with $a_\oplus \in [0.5,\, 2]\,\mathrm{mm/s^2}$ and $V_\infty \in [0,\, 1]\,\Delta V_H \simeq [0,\, 5.59]\,\mathrm{km/s}$, are summarized in Fig. 20(c). The minimum flight time t_f as a function of $a_\oplus$ and V_∞ is similar to that found for both Mercury and Venus. In particular, in this case for medium-high values of the characteristic acceleration ($a_\oplus > 1.5\,\mathrm{mm/s^2}$) the flight time is nearly insensitive to $a_\oplus$.

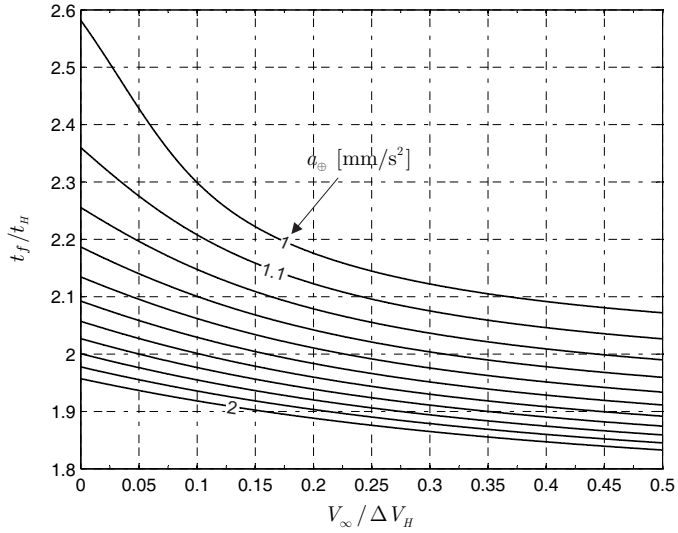

(a) Earth-Mercury transfer.

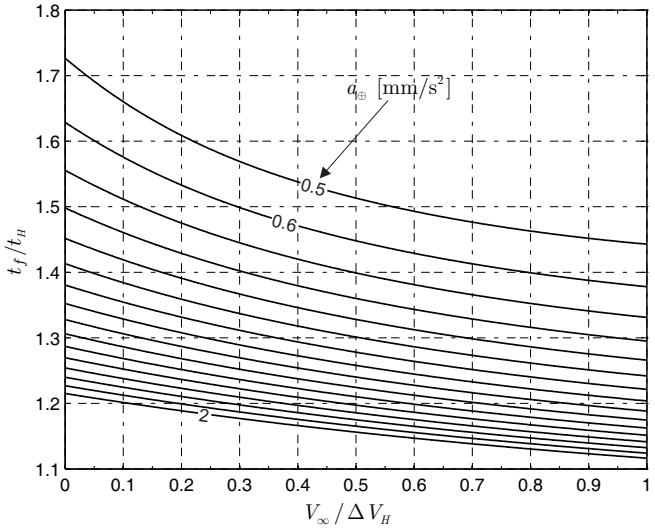

(b) Earth-Venus transfer.

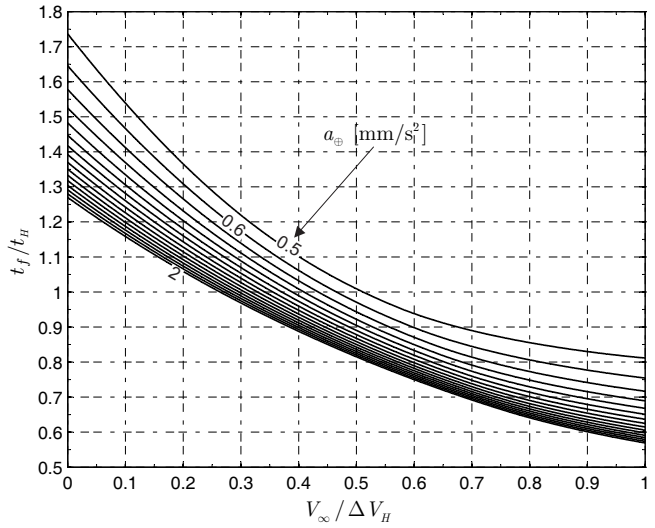

(c) Earth-Mars transfer.

Figure 20: Earth-inner planets minimum-time mission performance as a function of $a_\oplus$ and V_∞.

5.2 Missions toward outer planets

To obtain transfer trajectories with reasonable mission time, the analysis of missions toward outer planets is confined to characteristic accelerations ranging in the interval $[1,\, 2]\,\mathrm{mm/s^2}$ and hyperbolic excess speeds $V_\infty \in [0.5,\, 1]\,\Delta V_H$. The advantage of using an E-sail for flyby missions toward the outer planets is confirmed by Figs. 21 and 22, where the flight time is always less than $0.8\,t_H$.

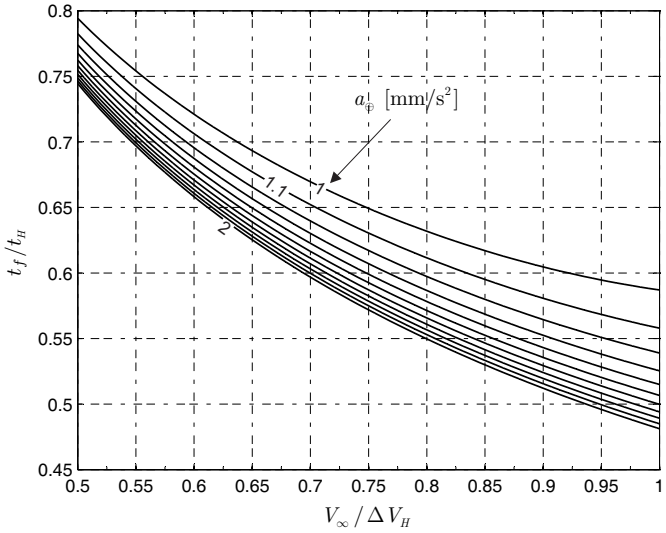

(a) Earth-Jupiter transfer.

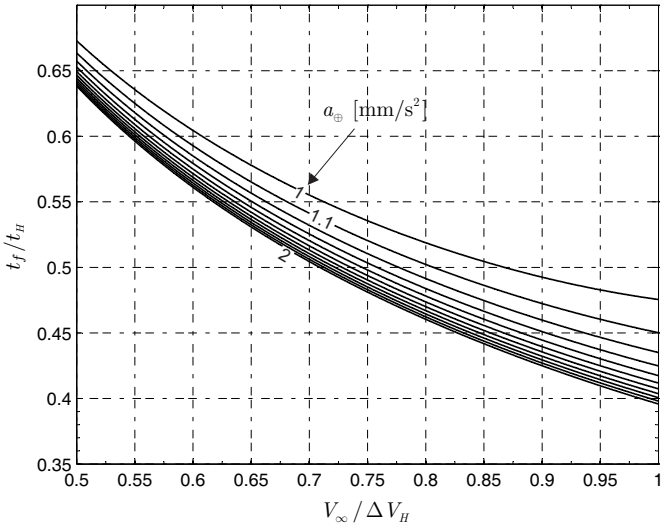

(b) Earth-Saturn transfer.

Figure 21: Earth-Jupiter/Saturn minimum-time mission performance as a function of $a_\oplus$ and V_∞.

When compared to the previous missions toward inner planets, the analysis of an Earth-Jupiter mission (see Fig. 21(a)) with a 2D approach provides rather accurate simulation results. This is due to the small values of the planet orbit eccentricity ($e \cong 0.04839$) and inclination ($i \cong 1.3\,\mathrm{deg}$). From Fig. 21(a), the flight time vary from about $2.15\,\mathrm{years}$ (for $V_\infty = 0.5\,\Delta V_H$) down to $1.6\,\mathrm{years}$ (for $V_\infty = \Delta V_H$). As long as transfers toward Saturn, Uranus, and Neptune are concerned, Figs. 21(b) and22 show similar trends.

In particular, note that the relationship between t_f/t_H and $V_\infty/\Delta V_H$ can be ap-

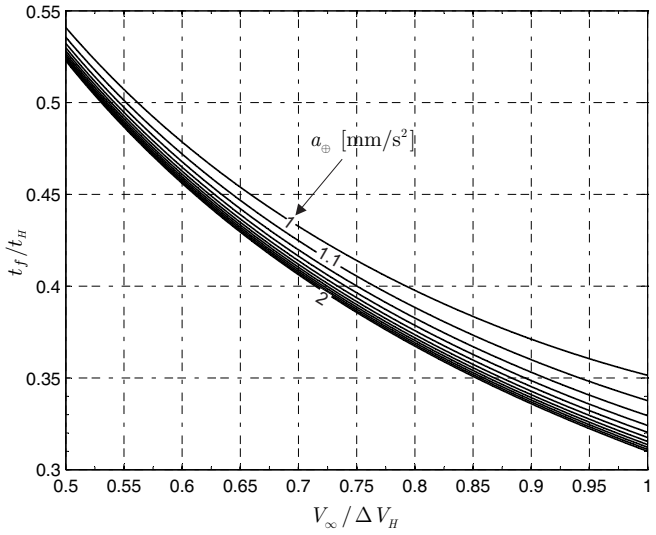

(a) Earth-Uranus transfer.

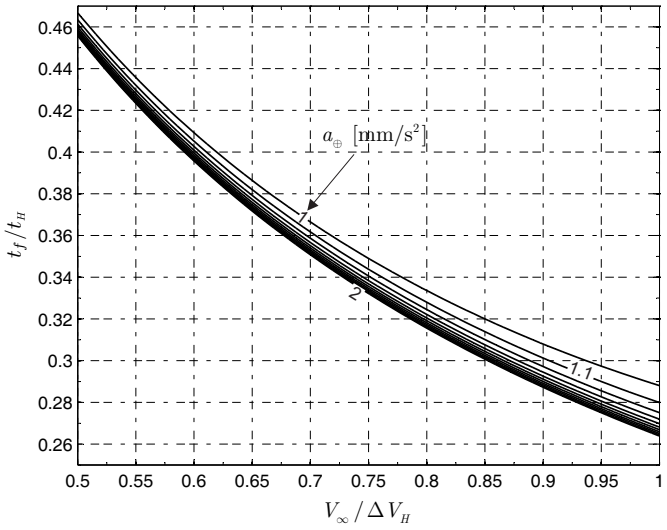

(b) Earth-Neptune transfer.

Figure 22: Earth-Uranus/Neptune minimum-time mission performance as a function of $a_\oplus$ and V_∞.

proximated for all the outer planets, with an error less than 10^{-3} , by the formula

$$\frac{t_f}{t_H} = b_1 \left(\frac{V_\infty}{\Delta V_H} \right)^{b_2} + b_3 \qquad \text{with} \qquad V_\infty \in [0.5,\, 1]\, \Delta V_H \tag{20}$$

where b_1, b_2, and b_3 are suitable interpolating coefficients, depending on the characteristic acceleration, and whose values are shown in Table 3.

Two examples of optimal trajectory and control laws for an E-sail transfer toward Jupiter are illustrated in Fig. 23, assuming $a_c = 1\,\mathrm{mm/s^2}$ and two different values of the hyperbolic excess velocity. Note that the value of V_∞ remarkably affects the thrusting time. In fact Fig. 23 shows that if the hyperbolic excess velocity is varied from $V_\infty = 0.5\,\Delta V_H$ to $V_\infty = \Delta V_H$, the thrusting time increases from 31.5% to 80% of the flight time.

Planet	$a_\oplus$ [mm/s^2]	b_1	b_2	b_3
Jupiter	1.0	0.1288	−1.3980	0.4569
	1.5	0.2929	−0.8913	0.2138
	2.0	0.3217	−0.8588	0.1598
Saturn	1.0	0.1404	−1.284	0.3328
	1.5	0.3172	−0.7988	0.0945
	2.0	0.344	−0.7682	0.0519
Uranus	1.0	0.196	−0.9835	0.1541
	1.5	0.3133	−0.7379	0.0042
	2.0	0.3273	−0.7221	−0.0172
Neptune	1.0	0.2129	−0.8835	0.0746
	1.5	0.2911	−0.7249	−0.0230
	2.0	0.2996	−0.7141	−0.0357

Table 3: Fitting coefficients (see Eq. (20)).

5.3 Performance comparison

A simple analysis in terms of required velocity variations and dry mass can be established by comparing a chemical propulsion based spacecraft and a hybrid configuration that combines a chemical thruster with an E-sail.

To this end, assume that the spacecraft is initially placed on a circular parking orbit around the Earth with an altitude $h_c = 200\,\mathrm{km}$ and that the capture orbit around the target planet is characterized by an altitude $h_p = 1\,000\,\mathrm{km}$. Consider a two-dimensional trajectory described through a patched conic approximation and a biimpulsive transfer. The first velocity variation ΔV_{esc} is employed to leave the parking orbit, while the second ΔV_{cap} is used to close the orbit around the target planet. The required total variation of velocity, ΔV_{tot}, is the sum of ΔV_{esc} and ΔV_{cap}. Assuming for the hybrid configuration $V_\infty = \Delta V_H/2$ (see Table 2) and $a_\oplus = 1\,\mathrm{mm/s^2}$, the simulation results have been summarized in Table 4 and compared with the results corresponding to a biimpulsive transfer with a Hohmann heliocentric trajectory. Note that for a hybrid propulsion system ΔV_{esc} is constant because, by assumption, the E-sail follows an escape parabolic orbit with respect to the Earth.

Table 4 shows that the hybrid configuration guarantees a substantial reduction in the required total velocity variation with respect to the Hohmann transfer for missions toward Mercury and outer planets. For example, a mission to Neptune guarantees a ΔV_{tot} saving of 47% and even a flight time decrease of $15\,\mathrm{years}$ when compared to a Hohmann transfer. Note however that such a performance increase for a hybrid configuration (in particular, the ΔV_{tot} saving) does not imply a proportional increase of the corresponding dry mass fraction deliverable.

The latter point can be better discussed by using a simplified mass breakdown model to obtain an estimate of the dry mass of the spacecraft (see Refs. [23] and [AD5], for details). According to the model, the spacecraft launch mass m_0 is obtained as the sum of three contributions: 1) the dry mass m_{dry} (which coincides with the spacecraft mass at the end of the capture phase), 2) the E-sail mass m_{sail} (comprising the structural mass necessary to join the probe with the sail), and 3) the

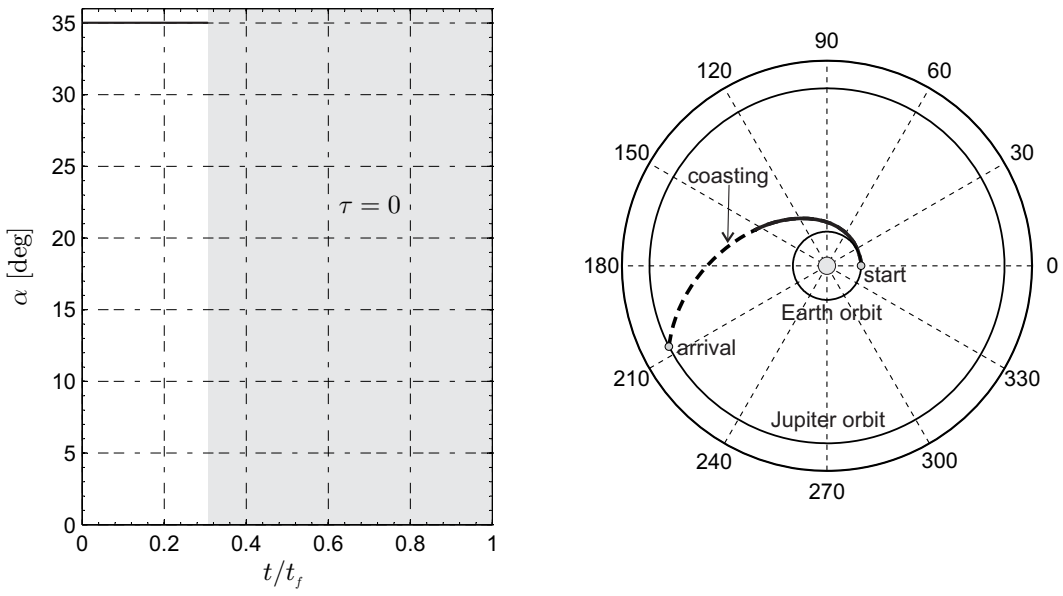

(a) $V_\infty = 0.5\,\Delta V_H \simeq 7.22\,\mathrm{km/s}$

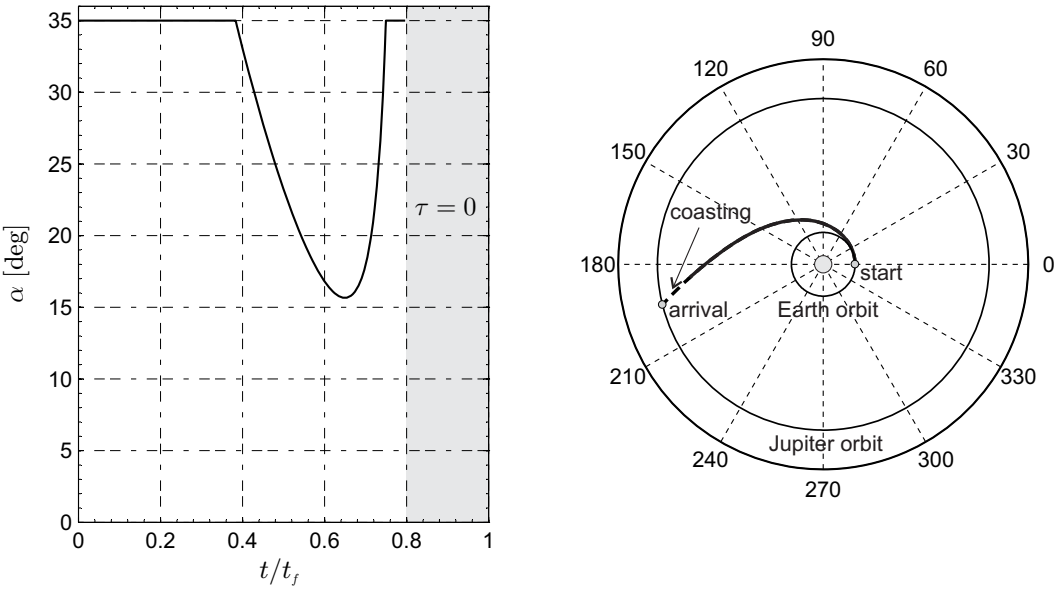

(b) $V_\infty = \Delta V_H \simeq 14.43\,\mathrm{km/s}$

Figure 23: Earth-Jupiter optimal trajectory and control angle time history ($a_\oplus$ = 1 mm/s^2).

propellant mass m_{prop} required by the chemical thrusters. Note that the chemical propulsion system is part of the dry mass.

The model shows that, with the same values of launch mass and specific impulse, the dry mass fraction concerning the hybrid solution $\sigma_{\mathsf{dry_E}}$ is greater than the dry mass fraction concerning the chemical solution $\sigma_{\mathsf{dry_C}}$ provided that the spacecraft mass fraction $\sigma_{\mathsf{sail}} \triangleq m_{\mathsf{sail}}/m_0$ is less than a critical value $\sigma^\star_{\mathsf{sail}}$.

The critical spacecraft mass fraction $\sigma^\star_{\mathsf{sail}}$ is directly related with the characteristic acceleration $a_\oplus$ and the minimum flight time t_f. Therefore, a graphical representation can be given once that the target planet is given. For example, Fig. 24 shows the contours of $\sigma^\star_{\mathsf{sail}}$ as a function $a_\oplus$ and t_f for an Earth-Jupiter transfer. Assuming a flight time $t_f = 2\,\mathrm{years}$ and a characteristic acceleration $a_\oplus = 1\,\mathrm{mm/s^2}$, the hybrid

Planet	Hohmann transfer				Hybrid option				
	ΔV_{esc} [km/s]	ΔV_{cap} [km/s]	ΔV_{tot} [km/s]	t_H [years]	ΔV_{esc} [km/s]	ΔV_{cap} [km/s]	V_∞ [km/s]	ΔV_{tot} [km/s]	t_f [years]
Mercury	5.554	6.677	12.232	0.289	3.224	5.710	8.572	8.934	0.598
Venus	3.503	0.374	3.878	0.399	3.224	0.346	2.601	3.570	0.520
Mars	3.611	0.733	4.344	0.708	3.224	0.811	2.796	4.035	0.631
Jupiter	6.305	0.266	6.571	2.731	3.224	0.434	7.218	3.658	2.155
Saturn	7.284	0.411	7.695	6.046	3.224	0.854	7.865	4.078	4.001
Uranus	7.978	0.511	8.489	16.039	3.224	1.463	7.970	4.688	8.653
Neptune	8.247	0.353	8.600	30.613	3.224	1.298	7.853	4.523	14.127

Table 4: Biimpulsive interplanetary transfer ΔV budget: chemical vs hybrid performance (with $a_\oplus = 1$ mm/s^2 and $V_\infty = \Delta V_H/2$).

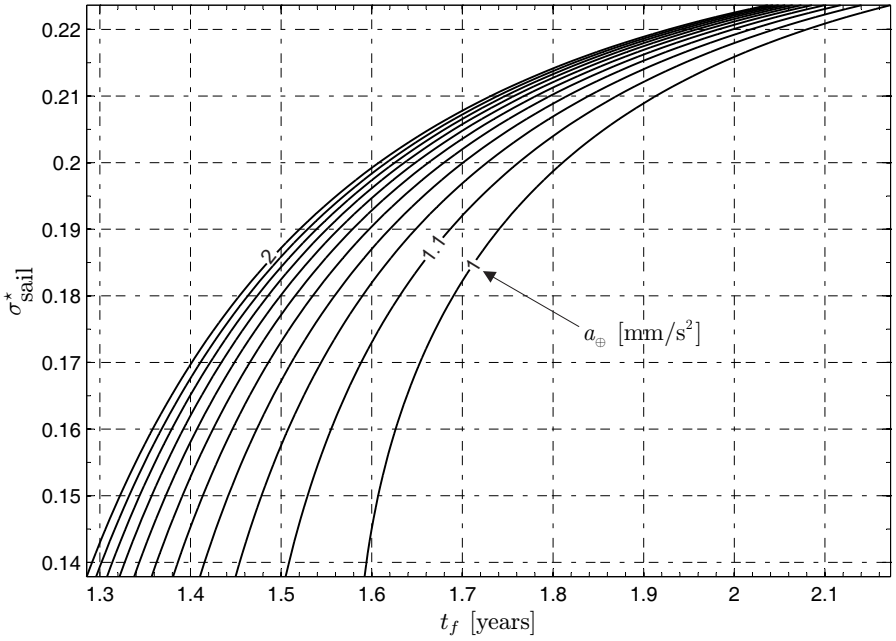

Figure 24: E-sail critical mass fraction $\sigma^\star_{\text{sail}}$ for an Earth-Jupiter transfer with $I_{sp} = 350\,\text{s}$.

option provides a dry mass fraction deliverable greater than that corresponding to a chemical case provided that the sail mass fraction is less than 0.216. Qualitatively similar results are obtained by studying transfers toward the other outer planets.

6 Missions toward asteroids

After the pioneering successes of the American mission Near Earth Asteroid Rendezvous – Shoemaker and the more recent conclusion of Japanese Hayabusa mission, the scientific community has renewed its interest in studying those minor celestial bodies that populate the interplanetary space surrounding Earth. Certainly, the two new European missions Don Quijote and Marco Polo are expected to represent a fundamental step forward in the knowledge of these interesting celestial bodies of the SS.

The E-sail represents an interesting option for missions toward asteroids, because its peculiar characteristics allow the spacecraft to fulfill transfers that otherwise will need either a considerable propellant mass [24] or significant complications such as planetary flybys [25–27]. Moreover, unlike conventional chemical propulsion systems [28], an E-sail offers some flexibility in the selection of the launch window, a feature that may be obtained also with a solar sail [29–32] and, to a lesser extent, with an electric propulsion system [33] and a mini-magnetospheric plasma thruster [34, 35].

6.1 Missions toward Potentially Hazardous Asteroids

A fraction of the whole population of asteroids and comets, referred to as Potentially Hazardous Asteroids (PHAs), is known to be potentially perturbed into orbits that may cross the Earth's orbit. The potential threat posed by these objects of colliding with Earth may be so catastrophic that it is important to quantify the risk and prepare to deal with such a threat [36].

Although the annual likelihood that PHAs collide with Earth is extremely small [37], it is important to investigate mission scenarios whose purpose is to send a spacecraft near the asteroid [38, 39] to leave it a transponder (or a reflector). In fact, tagging the asteroid may be necessary to track it accurately enough to determine the probability of a collision with Earth, and thus help to decide whether to mount a deflection mission to alter its orbit.

In this section, we provide a thorough analysis of E-sail potentialities to perform rendezvous missions toward any of the current catalogued PHAs (a total of 1025). The problem has been addressed within a 3D framework by introducing modified equinoctial elements into the equations of motion to reduce the computational time required by simulations, see Ref. [AD6] for details.

The E-sail provides the acceleration defined by Eq. (1) with $d \equiv 1\,\mathrm{au}$, $\eta = 7/6$, and $\alpha_{\max} = 30\,\mathrm{deg}$. A reference value of characteristic acceleration of $1\,\mathrm{mm/s^2}$ was assumed for all of the simulations. At the initial time instant $t_0 \triangleq 0$, the spacecraft position is generically identified by the true anomaly ν_0 on an orbit around the Sun coincident with the Earth's elliptical heliocentric orbit, whereas at the end of the transfer $t = t_1$ the spacecraft is at the true anomaly ν_1 on the target orbit. The problem considered is to find the minimum time trajectory required by an E-sail to reach the orbit of each asteroid belonging to the set of known PHAs.

6.1.1 Optimal two-impulse transfers

To quantify the cost of a rendezvous mission toward the various PHAs, the total minimum ΔV variation ($\Delta V_{\min}$) for a two-impulse transfer has been preliminarily calculated. The value of $\Delta V_{\min}$ was obtained by solving a classical targeting problem between a point belonging to the Earth's heliocentric orbit (whose position is defined by the true anomaly $\nu_0 \in [0,\, 2\,\pi]$) and a second point belonging to the final orbit (characterized by the true anomaly $\nu_1 \in [0,\, 2\,\pi]$).

The simulation results have been compared and validated with those calculated by the *Advanced Concept Team* of the European Space Agency. The value of $\Delta V_{\min}$, along with the optimal initial and final angular positions of the spacecraft, are graphically summarized in Fig. 25 in terms of cumulative percent and are partially shown in the Table 5, for a complete list see Ref [AD6] 📌 . Without using supplementary maneuvers, the minimum ΔV required for a rendezvous mission is always greater than $3.5\,\mathrm{km/s}$ and less than $30\,\mathrm{km/s}$. From Fig. 25, about 48% of the PHAs population requires a $\Delta V_{\min}$ less than $10\,\mathrm{km/s}$, while only 17% require a $\Delta V_{\min}$ greater than $15\,\mathrm{km/s}$.

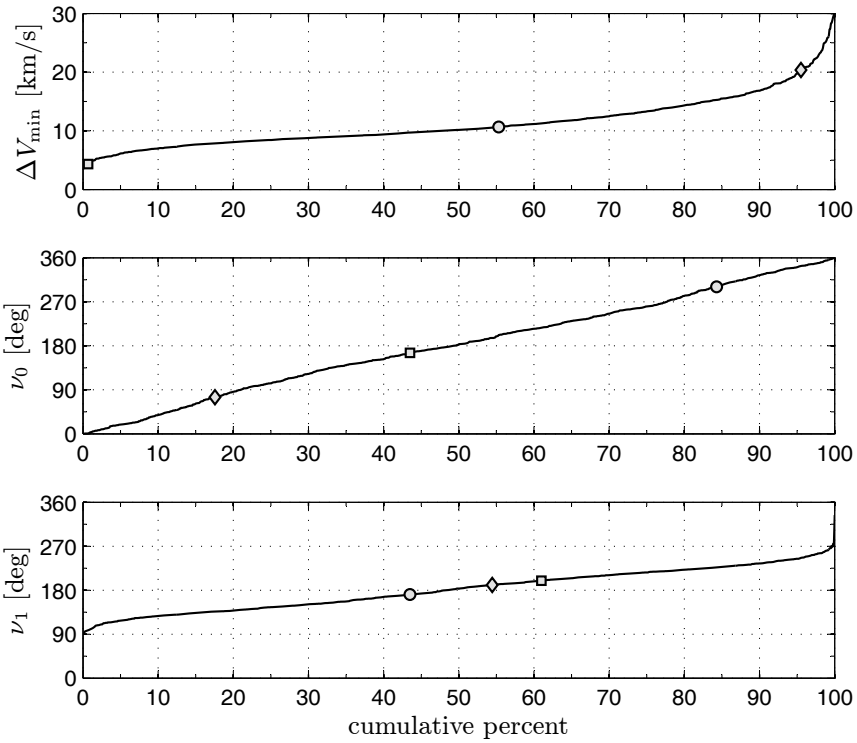

Figure 25: Performance of an Earth-PHA optimum two-impulse transfer ($\square = 99942$ Apophis, $\diamondsuit = 3200$ Phaethon, $\circ = 2101$ Adonis).

Table 5: Earth-PHA minimum transfer times for rapid missions ($t_1 \leq 180\,\mathrm{days}$). (Excerpt, for a complete list see Ref [AD6])

Asteroid name	Two-impulse transfer			E-sail transfer		
	$\Delta V_{\min}$ [km/s]	ν_0 [deg]	ν_1 [deg]	t_1 [days]	ν_0 [deg]	ν_1 [deg]
25143 Itokawa (1998 SF36)	4.252	132.0	210.5	86.87	139.8	88.0
(2002 AW)	4.121	165.8	195.1	87.60	227.6	127.4
(2006 KV89)	5.255	86.9	136.1	87.80	96.3	117.1
65679 (1989 UQ)	4.193	114.3	174.4	89.16	176.7	161.7
3361 Orpheus (1982 HR)	5.269	15.2	218.0	101.34	58.3	118.1
4660 Nereus (1982 DB)	4.968	10.7	219.1	101.77	6.1	88.0
(2002 RW25)	4.957	127.8	177.3	102.23	159.1	184.1
138404 (2000 HA24)	4.880	333.9	204.6	102.45	26.1	126.8
164202 (2004 EW)	5.744	335.4	147.1	102.79	355.2	148.0
99942 Apophis (2004 MN4)	4.335	165.6	199.6	106.85	297.5	164.4
(2004 PJ2)	5.836	131.8	237.3	107.55	142.7	98.3
(2000 SL10)	5.444	193.5	140.5	107.95	193.4	101.9
85585 Mjolnir (1998 FG2)	6.391	336.7	230.2	109.54	13.7	114.2
(2000 EA14)	3.566	305.5	144.2	111.48	323.8	116.3
(2003 YX1)	6.252	272.0	157.1	111.75	285.2	171.4
(2002 NV16)	3.672	259.3	189.1	112.99	253.4	93.6
(2000 QK130)	5.661	157.9	128.2	114.22	162.9	120.8

Asteroid name (continued)	Two-impulse transfer $\Delta V_{\min}$ [km/s]	ν_0 [deg]	ν_1 [deg]	E-sail transfer t_1 [days]	ν_0 [deg]	ν_1 [deg]
138175 (2000 EE104)	6.781	155.5	209.7	115.88	253.6	148.3
163364 (2002 OD20)	6.701	93.2	128.5	118.62	87.4	113.7
85990 (1999 JV6)	6.551	293.8	146.8	119.34	307.7	150.8
(2005 EE)	7.119	256.0	221.9	121.24	322.6	133.4
4581 Asclepius (1989 FC)	7.120	17.2	151.4	121.37	24.9	151.7

6.1.2 Minimum-time transfers with a_c= 1 mm/s^2

Using, as stated, a characteristic acceleration of $1\,\mathrm{mm/s^2}$, the results obtained in terms of minimum flight times and optimal initial and final angular positions are summarized in graphical form, in terms of cumulative percent, in Fig. 26. Details are also partially given in Table 5. For the whole population of PHAs the flight times are always

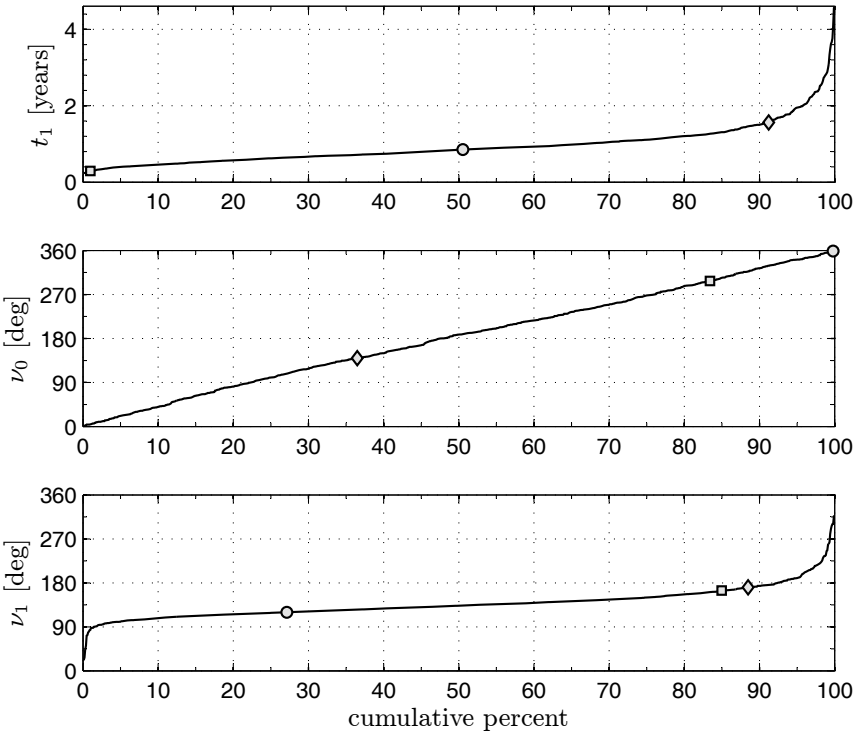

Figure 26: Minimum-time Earth-PHA transfer using E-sail with $a_c = 1$ mm/s^2 ($\square = 99942$ Apophis, $\lozenge = 3200$ Phaethon, $\circ = 2101$ Adonis).

less than $4.6\,\mathrm{years}$. This is a reasonable time, even the more so recalling that the missions are completed without any intermediate flyby maneuver. A noteworthy result is that about 67% of PHAs may be reached with a total mission time less than one year, while 4% only requires times greater than two years. Moreover, the E-sail has the potential to guarantee the fulfilment of rapid rendezvous missions, with times less than 180 days, to 137 asteroids, corresponding to about 14% of the whole population.

The potential of the E-sail for PHAs missions is also clearly shown in Fig. 27 in which, for each mission, the minimum flight time is represented as a function of the $\Delta V_{\min}$ found with a two impulse strategy. Figure 27 shows that the E-sail may reach, within reasonable times (that is, less than $4\,\mathrm{years}$), asteroids that otherwise would require $\Delta V_{\min} \simeq 30\,\mathrm{km/s}$, a value comparable to the Earth's mean orbital velocity.

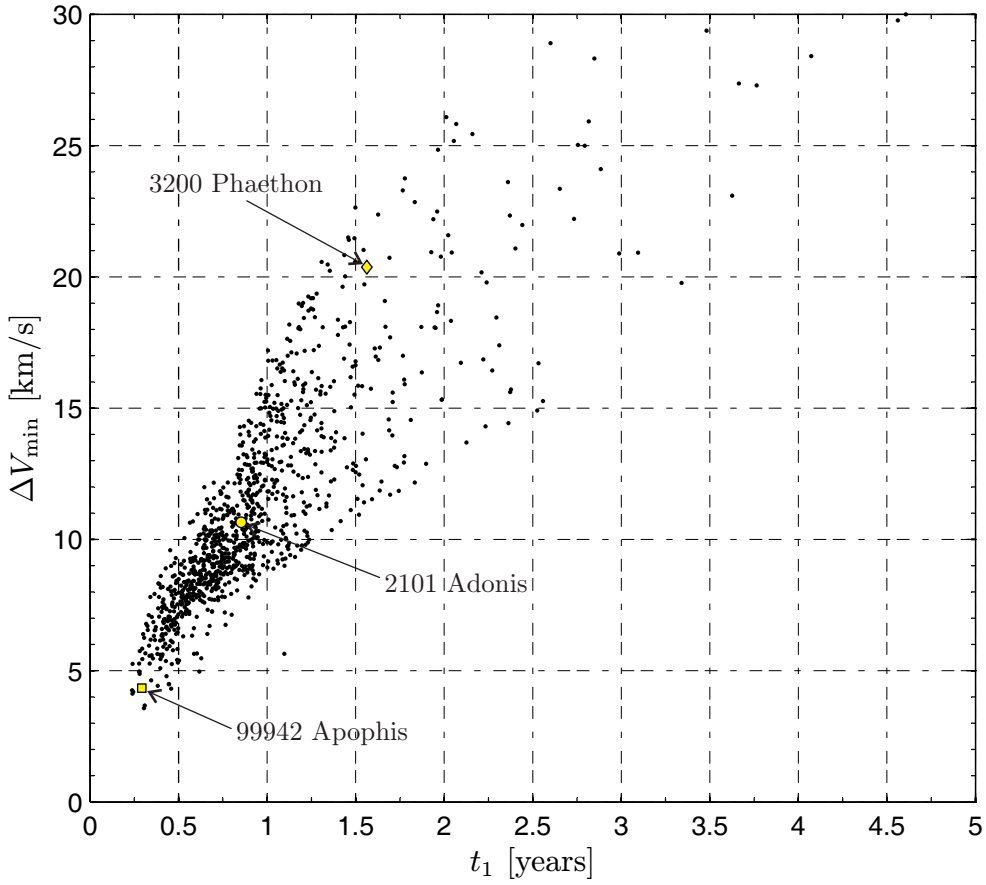

Figure 27: E-sail minimum flight time (t_1) vs. two-impulse $\Delta V_{\min}$.

6.1.3 Case study: rendezvous with asteroid 99942 Apophis

A parametric investigation to analyze the E-sail capabilities (in terms of mission times) for different values of both the characteristic acceleration and the maximum cone angle can be accomplished by using asteroid 99942 Apophis as a reference case study. Assuming a variation range $a_c \in [0.5,\, 2]\,\mathrm{mm/s^2}$ and $\alpha_{\max} \in [15,\, 30]\,\mathrm{deg}$, the isocontour lines for the minimum flight times are illustrated in Fig. 28.

As it is clear from the figure, there is a strong dependence of t_1 from a_c, especially for $a_c < 0.7\,\mathrm{mm/s^2}$ (note, in fact, that the curves $t_1 = t_1(a_c)$ have a vertical asymptote when $a_c \to 0$). The flight time has a certain dependence on the maximum allowed value of the cone angle, however such a dependence is weak when $\alpha_{\max} > 20\,\mathrm{deg}$.

Using the same value of characteristic acceleration for a solar sail and an E-sail, it is possible to obtain a reasonable comparison between the performance of this two different propulsion systems in terms of mission times. Clearly, there exists a suitable pair $(a_c,\, \alpha_{\max})$ such that the minimum mission time t_1 concerning the E-sail is equal to the minimum mission time $t_{1_{ss}}$ concerning the solar sail. The curve $a_c = a_c(\alpha_{\max})$ plotted in Fig. 29 characterizes all the pairs $(a_c,\, \alpha_{\max})$ such that the E-sail is superior, in terms of shorter mission times, to a flat solar sail (gray region) with an optical force model.

An example of transfer trajectory for an E-sail toward 99942 Apophis is illustrated in Fig. 30, assuming $a_c = 1\,\mathrm{mm/s^2}$ and $\alpha_{\max} = 30\,\mathrm{deg}$. Figure 30(b) shows the existence of a coasting phase ($\tau = 0$) of about $15\,\mathrm{days}$. This is confirmed by Fig 31 where the control angles are illustrated.

To conclude, assuming to fix the initial spacecraft position ν_0 on the initial orbit,

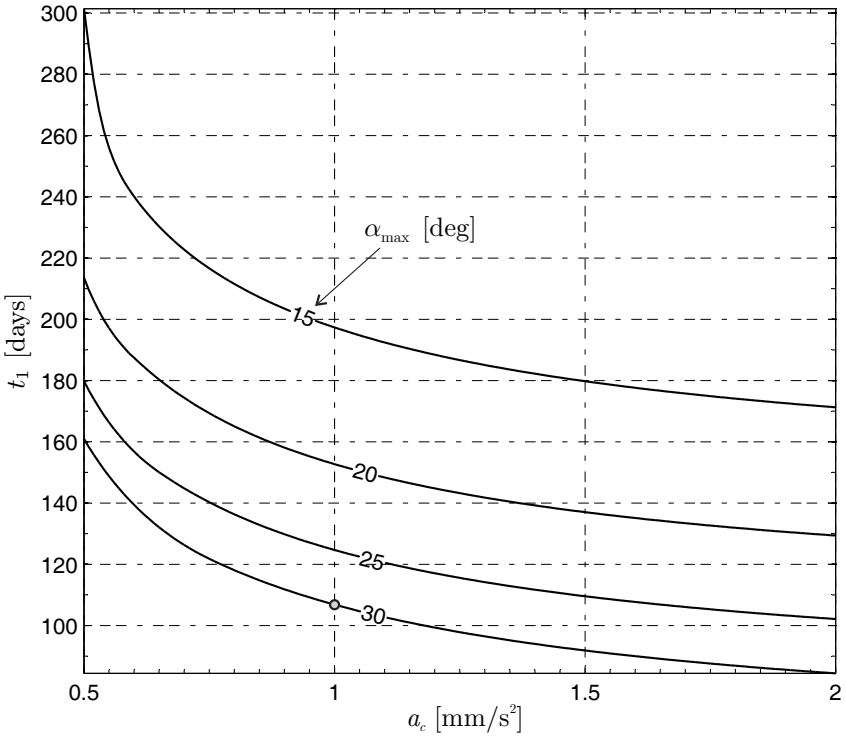

Figure 28: Mission toward asteroid 99942 Apophis: minimum transfer times t_1 as a function of a_c and $\alpha_{\max}$. The gray point represents the case discussed in the text.

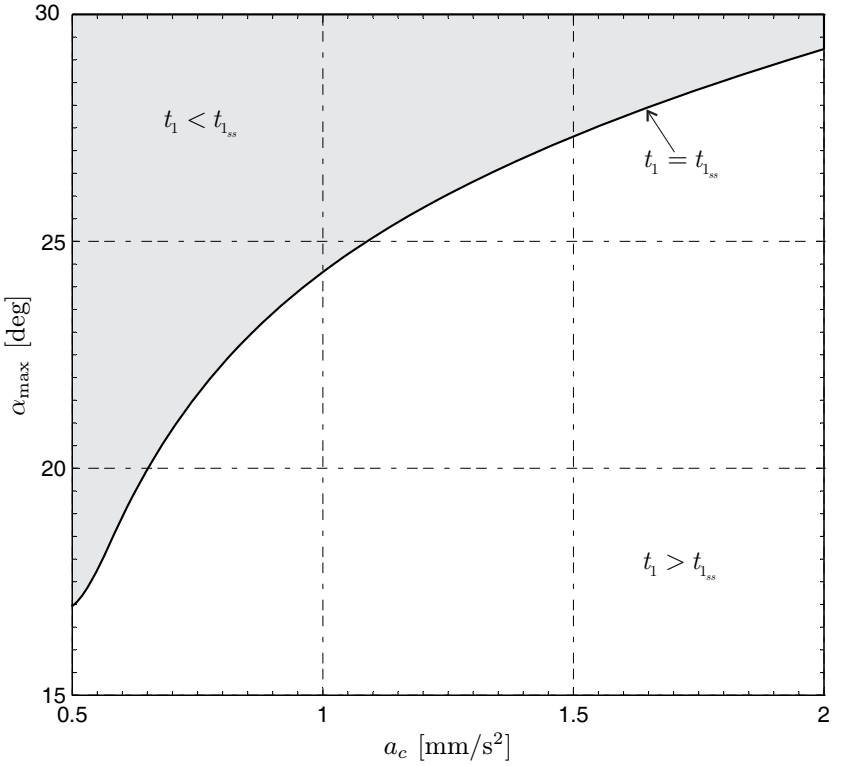

Figure 29: E-sail vs. solar sail performance for minimum-time mission toward asteroid 99942 Apophis.

it is possible to calculate the optimal mission performance assigning a launch date. When the optimal control problem is solved for different values of the characteristic

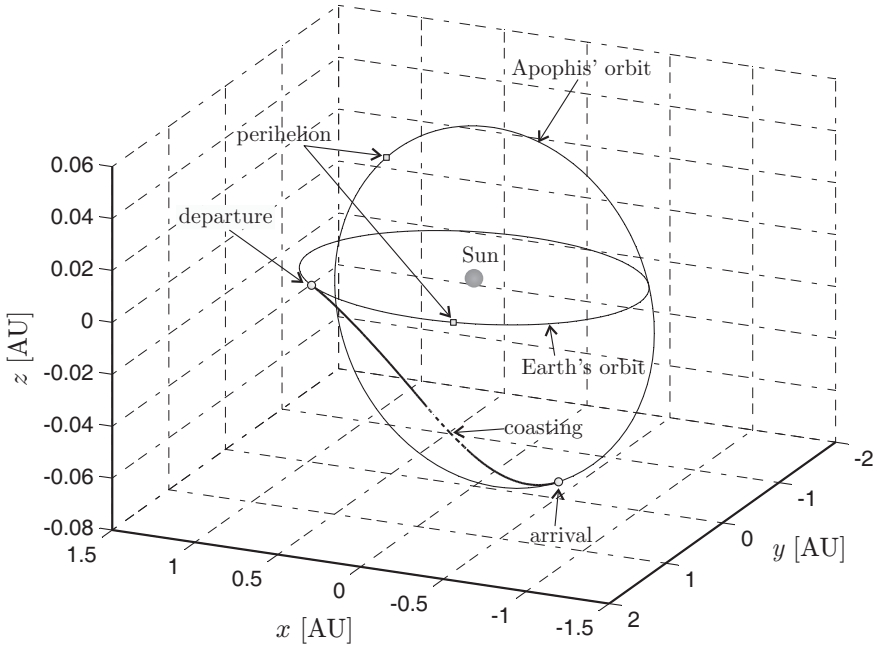

(a) Three-dimensional view.

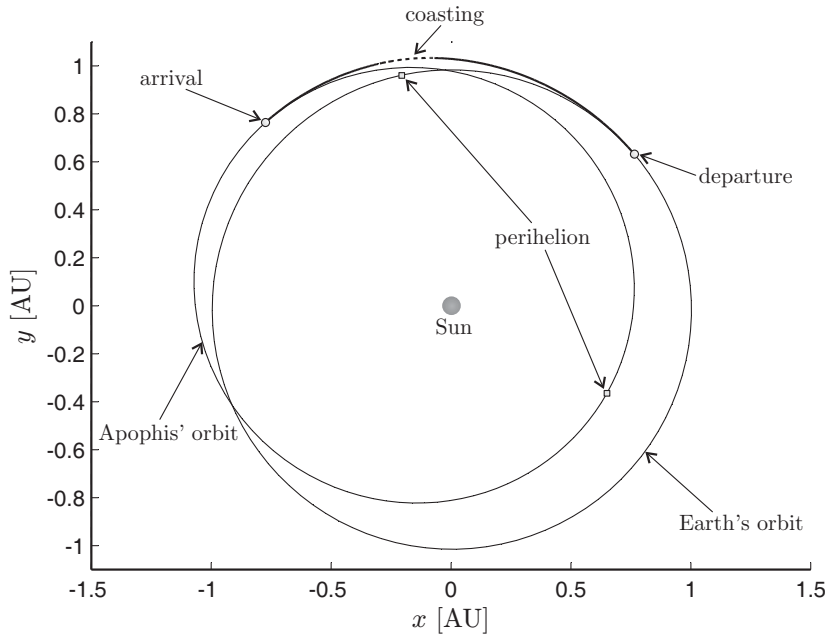

(b) Ecliptic projection.

Figure 30: Optimal Earth-Apophis ephemeris-free trajectory with $a_c = 1$ mm/s^2 and $\alpha_{\max} = 30$ deg.

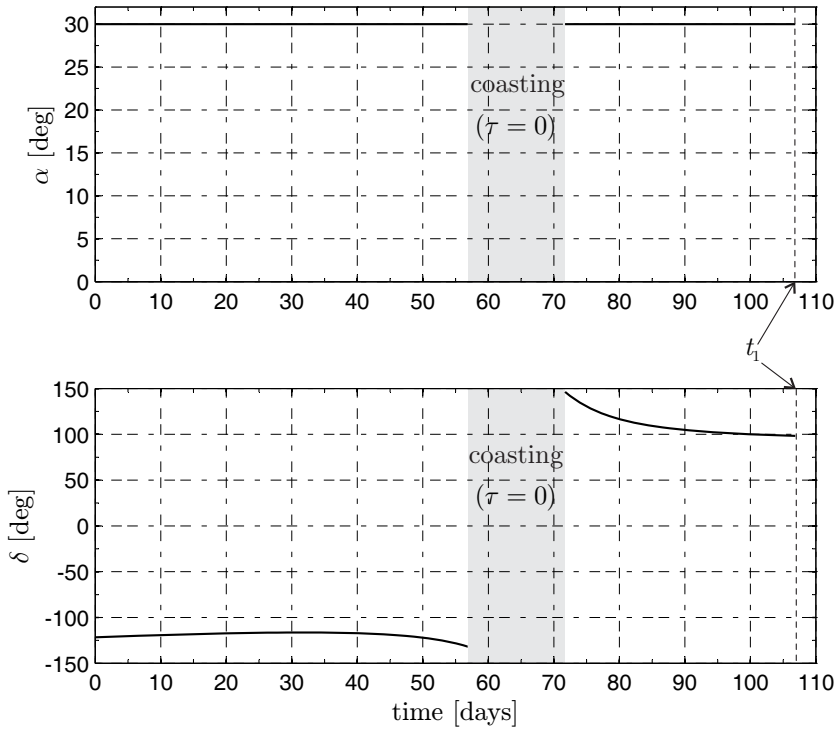

Figure 31: Mission toward 99942 Apophis: optimal control angles ($a_c = 1$ mm/s^2 and $\alpha_{\max} = 30$ deg).

acceleration and $\alpha_{\max} = 30\,\mathrm{deg}$, the simulation results are illustrated in Fig. 32.

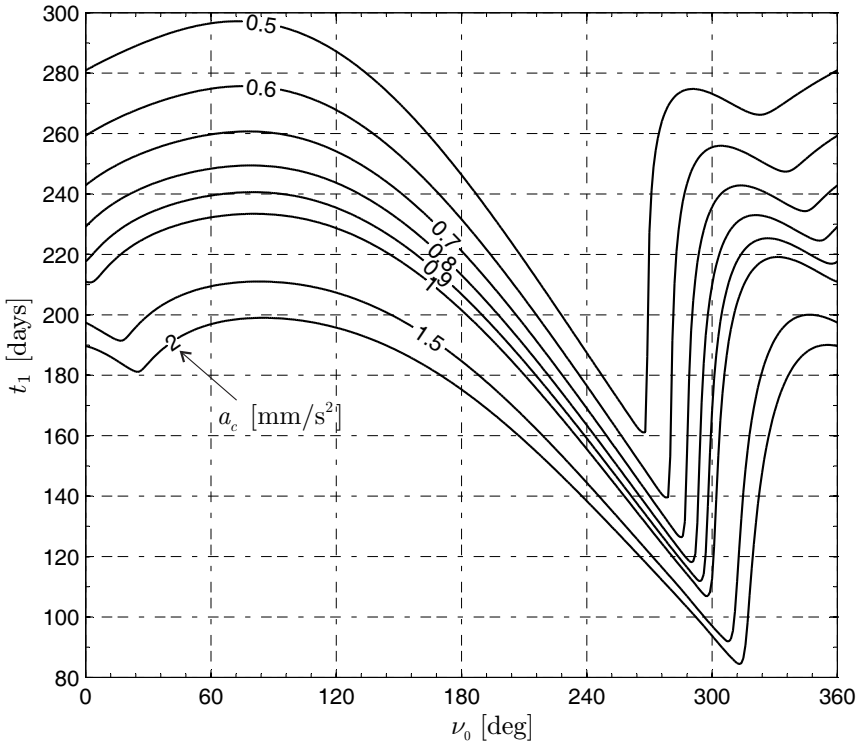

Figure 32: Mission toward asteroid 99942 Apophis: minimum transfer time t_1 as a function of a_c and ν_0 ($\alpha_{\max} = 30$ deg).

For a given value of a_c, the curve $t_1 = t_1(\nu_0)$ shows the presence of both a local

and a global minimum. The latter value is coincident with the results of Fig. 28 and of Table 5.

6.2 Nodal flyby with Near-Earth Asteroids

In general terms, an orbital rendezvous with a Near-Earth Asteroid (NEA) using a robotic mission is a rather involved problem, due to the typical non-negligible orbital inclination of those (minor) celestial bodies. For example, about 49% of the currently known NEAs, have a heliocentric orbital inclination greater than $10\,\mathrm{deg}$. Such a characteristic, especially when coupled with a non-negligible value of orbital eccentricity, in most cases requires the need of a large ΔV to perform a classical rendezvous mission with a high-thrust propulsion system as, for example, a chemical rocket. A substantial reduction of the necessary ΔV can be obtained by relaxing the constraints regarding the terminal phase of the mission, for example by performing a close encounter with the asteroid instead of an orbital rendezvous. Within the context of flyby missions toward NEA, Ref. [40] discusses an interesting approach, referred to as nodal flyby, in which the target asteroid is reached at one of its two orbital nodes using an impulsive transfer. A similar idea has been subsequently exploited in Ref. [41] to accomplish a preliminary mission analysis toward long-period comets with high orbital inclination and using a solar sail.

In our analysis all NEAs in the set of known asteroids (evaluated at mid-January 2013) have been taken into account as potential targets in a robotic mission scenario for an E-sail based spacecraft. The analysis of each mission case has been performed within an optimal framework, by calculating the minimum-time 2D trajectory necessary to reach one orbital node of the target asteroid. At the initial time instant $t_0 \triangleq 0$, the spacecraft is assumed to be on a heliocentric orbit coincident with the Earth's orbit, here considered circular. The latter is a common assumption that is usually adopted to obtain conservative results and to reduce the number of free parameters. However, the numerical simulations have shown that the actual eccentricity of the terrestrial orbit has a negligible effect on the optimal flight time unless the characteristic acceleration takes very small values, see Ref. [AD7] for details. For all simulations, the E-sail is assumed to provide the acceleration defined by Eq. (1) with $d \equiv 1\,\mathrm{au}$, $a_c = 1\,\mathrm{mm/s^2}$, $\eta = 1$, and $\alpha_{\max} = 30\,\mathrm{deg}$.

Data regarding the whole set $\mathcal{J}$ of 9546 known NEAs have been retrieved from the JPL database[3]. Considering the solar distances r_f of both orbital nodes of each asteroid in the set $\mathcal{J}$, the corresponding minimum time trajectory required to attain a nodal flyby has been calculated. The simulation results, including the minimum flight time t_f and the polar angle $\Delta\theta$ swept by the spacecraft along the whole transfer trajectory, have been collected in a database attached to Ref. [AD7] 📌 . An excerpt of the results obtained is shown in Table 6.

Figure 33 summarizes the performance of an E-sail, showing the required minimum mission times necessary to reach a NEA in terms of cumulative percent. For each asteroid, the target node corresponds to the solution (that is, ascending or descending node) that minimizes the mission time. Figure 33 shows that over 60% of NEAs can be reached with a total mission time less than $100\,\mathrm{days}$. The same figure also highlights four particularly representative asteroids. Notably, all of the NEAs can be reached with a maximum flight time of about $300\,\mathrm{days}$. However, note that in Fig. 33 the spacecraft was assumed to start from Earth, and to reach a given target asteroid. In principle, in a multi-asteroid mission a somewhat faster asteroid visitation rate is expected to be possible, because the succeeding asteroid can be selected

[3] `http://neo.jpl.nasa.gov/cgi-bin/neo_elem` (retrieved at January 15, 2013)

Id	Asteroid name	Descending Node			Ascending Node		
		r_f [au]	$\Delta\theta$ [deg]	t_f [days]	r_f [au]	$\Delta\theta$ [deg]	t_f [days]
1	433 Eros (1898 DQ)	1.1335	65.8856	69.33	1.7823	130.2887	177.8429
2	719 Albert (1911 MT)	1.2154	80.6579	87.823	3.6821	179.097	408.7889
3	887 Alinda (1918 DB)	3.8124	180.706	423.33	1.0768	51.6046	53.1307
4	1036 Ganymed (1924 TD)	1.3981	102.8209	120.89	2.9788	168.1276	328.0322
5	1221 Amor (1932 EA1)	2.546	158.5202	276.1	1.1193	62.7493	65.6545
6	1566 Icarus (1949 MA)	1.1603	71.2667	75.822	0.1998	x	x
7	1580 Betulia (1950 KA)	1.1483	68.9397	72.984	3.0818	170.0316	340.1202
8	1620 Geographos (1951 RA)	1.151	69.4866	73.647	1.0629	47.1171	48.2819
9	1627 Ivar (1929 SH)	1.1308	65.2998	68.638	2.5633	158.9632	278.2145
10	1685 Toro (1948 OA)	0.8766	144.4255	158.1	1.5027	112.0384	137.4491

Table 6: Simulation results obtained for sample NEAs with $a_c = 1$ mm/s^2. (Excerpt)

within a set of suitable targets in each phase of the mission.

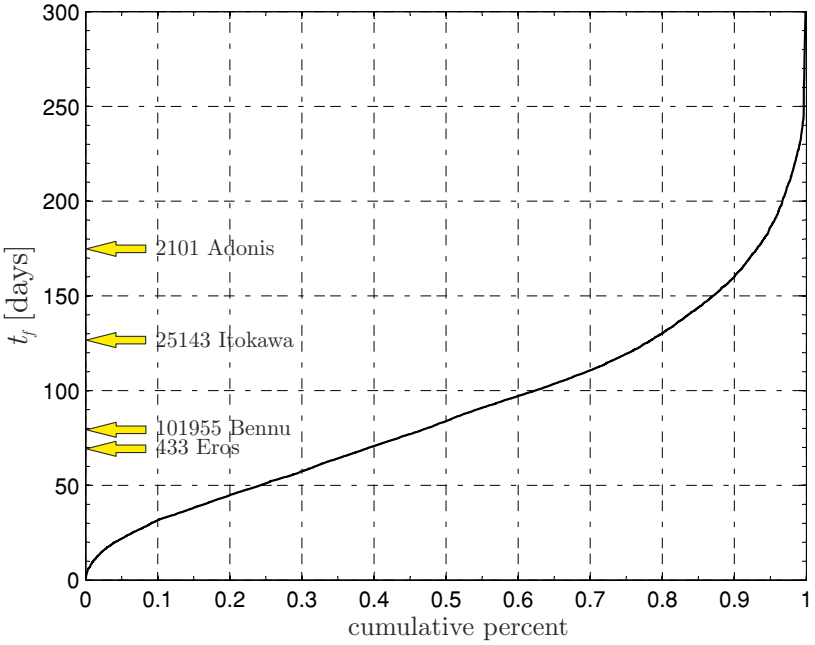

Figure 33: Performance of an Earth-NEA optimum E-sail transfer ($a_c = 1$ mm/s^2).

6.3 Sample return mission toward 1999 KY26

The successful conclusion of Japanese Hayabusa mission, which, on 13 June 2010, returned to Earth with a material sample from asteroid 25143 Itokawa has first demonstrated the technical feasibility of retrieving material samples from a NEA. This new frontier will be further advanced by Origins-Spectral Interpretation-Resource Identification- Security- Regolith Explorer (OSIRIS-REx) mission whose aim is to reach asteroid 1999 RQ36 in 2019.

In this section, the 1998 KY26 is chosen as a representative NEA candidate target for the preliminary design of a sample return mission for a spacecraft, whose primary propulsion system is an E-sail. The mission is analyzed to find the minimum total flight time as a function of the E-sail characteristic acceleration, using the propulsive acceleration model given in Eq. (1) with $d = 1\,\mathrm{au}$, $\eta = 1$, and $\alpha_{\max} = 30\,\mathrm{deg}$. The optimal trajectories have been calculated assuming the spacecraft at the initial time

instant is on the Earth’s elliptical heliocentric orbit and using a direct transfer (that is, without gravity assist maneuvers) between the two celestial bodies. The heliocentric orbital parameters of Earth and asteroid 1998 KY26 have been retrieved from JPL ephemerides [42, 43] and are summarized in Table 7. For further details, see Ref. [AD8].

orbital element	Earth+Moon barycenter	asteroid 1998 KY26
semimajor axis [au]	9.99996×10^{-1}	1.23199
eccentricity	1.66928×10^{-2}	2.01378×10^{-1}
inclination [deg]	1.66709×10^{-3}	1.48113
long. of asc. node [deg]	176.223	84.4464
arg. of per. [deg]	286.744	209.182
mean anomaly [deg]	356.926	306.675

Table 7: Reference orbital elements at MJD $= 55927$ (January 1, 2012).

The whole space mission can be ideally divided into three phases, as is schematically shown in Fig. 34. In a first transfer phase, whose time length is Δt_{EA}, the spacecraft is transferred from the Earth’s heliocentric orbit to the asteroid’s orbit. At the end of this phase the spacecraft concludes its rendezvous maneuver with the target asteroid and maintains a prescribed orbit relative to it. In the second phase, referred to as scientific phase, the spacecraft completes the prescribed scientific measurements. The time interval of this second phase is Δt_w (waiting time). In this phase a lander can be used to possibly reach the asteroid’s surface and collect material samples. At the end of the second phase the lander (or part of it) performs a docking maneuver with the E-sail based spacecraft. The third phase starts at the docking instant and ends with an Earth’s rendezvous (with no hyperbolic excess), within a time interval of Δt_{AE}. According to this simplified model the total mission time Δt is

$$\Delta t = \Delta t_{\mathsf{EA}} + \Delta t_w + \Delta t_{\mathsf{AE}}. \tag{21}$$

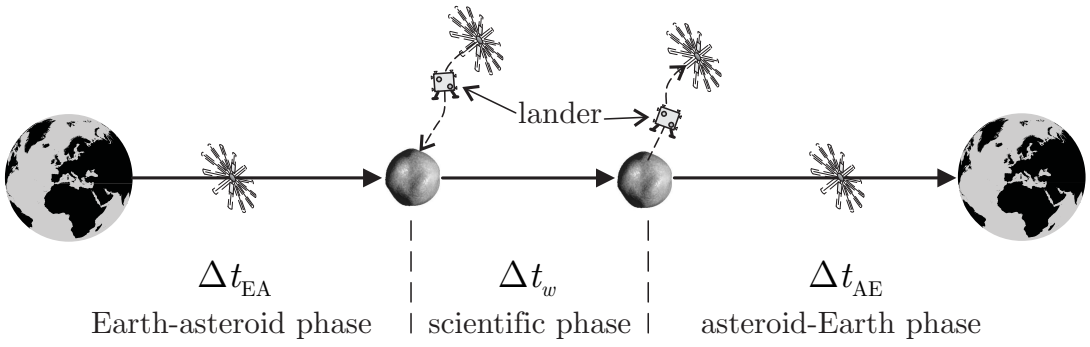

Figure 34: Schematic view of sample return mission phases.

For a given value of spacecraft characteristic acceleration $a_c \triangleq a_\oplus$, the flight times for the first and last mission phases are calculated by minimizing the time interval required for the rendezvous-maneuvers (Earth-asteroid and asteroid-Earth phases). Accordingly, the two values $\Delta t_{\mathsf{EA}}(a_\oplus)$ and $\Delta t_{\mathsf{AE}}(a_\oplus)$ are calculated numerically as a function of the starting date of each phase in terms of Modified Julian Date (MJD).

6.3.1 Orbit-to-orbit optimal trajectories

Firstly, minimum time, 3D transfer trajectories have been calculated, for phases one and three, by neglecting any ephemeris constraint on the two celestial bodies. In other terms, within an orbit-to-orbit optimal trajectory, the spacecraft matches the (Keplerian) heliocentric orbit of the two celestial bodies at both departure and arrival time instants. This implies that only the shape and orientation of the two orbits (corresponding to the data of Table 7) are taken into account in the optimization process.

The main results concerning the first mission phase have been summarized in Table 8, while Table 9 shows the corresponding results for the third (return) phase. The variable ν_i (or ν_f) represents the spacecraft heliocentric true anomaly along the starting (arrival) orbit at the initial (final) time instant. Recall that the spacecraft's starting and arrival orbit coincides with the heliocentric (Keplerian) orbit of one of the two celestial bodies of the problem. The fifth column of Tables 8 and 9 shows the number of complete revolutions around the Sun during the mission phase. Tables 8

$a_\oplus\,[\mathrm{mm/s^2}]$	$\Delta t_{\mathsf{AE}}\,[\mathrm{days}]$	$\nu_i\,[\mathrm{deg}]$	$\nu_f\,[\mathrm{deg}]$	revs.	$a_{\oplus_{ss}}\,[\mathrm{mm/s^2}]$
1	94.36	189.45	84.11	0	1.0883
0.9	97.85	188.24	85.87	0	1.0430
0.8	102.12	186.76	87.99	0	0.9937
0.7	107.44	184.92	90.59	0	0.94
0.6	118.92	181.49	96.39	0	0.8471
0.5	146.75	172.96	108.76	0	0.7009
0.4	200.91	156.65	129.55	0	0.5604
0.3	371.33	105.75	177.94	0	0.4578
0.2	568.89	170.42	110.35	1	0.2616
0.15	892.26	231.16	105.71	2	0.2161
0.14	929	205.72	105.32	2	0.2163
0.13	973.67	179.71	110.33	2	0.2159
0.12	1040.4	146.62	124.23	2	0.21
0.11	1211.3	106.24	176.75	2	0.1471
0.1	1347.9	204.23	106.98	3	0.1444
0.09	1449.8	152.32	122.22	3	0.1425

Table 8: Orbit-to-orbit optimal performance for Earth-asteroid transfer phase.

and 9 clearly show a rapid increase in the flight time by decreasing the spacecraft characteristic acceleration $a_\oplus$. Note that a rapid transfer to the asteroid 1998 KY26, that is, a mission whose transfer time is less than one terrestrial year [32], requires a characteristic acceleration $a_\oplus \geq 0.3\,\mathrm{mm/s^2}$. In this case, the mission is completed within less than a full revolution about the Sun, as is indicated by the fifth column of Table 8. Instead, if $a_\oplus < 0.3\,\mathrm{mm/s^2}$, the heliocentric trajectory is more involved, with multiple revolutions around the Sun, and the flight time increases up to exceeding four years if $a_\oplus < 0.09\,\mathrm{mm/s^2}$, see Table 8. A similar result holds for the return phase.

To better emphasize the capability of performing such a mission type, the performance of an E-sail can be compared to those of an ideal solar sail. The latter may be thought of as being equivalent to a perfectly reflecting flat surface. Assuming a flight time corresponding to the value necessary for an E-sail to complete the mission, it is possible to calculate the minimum characteristic acceleration $a_{\oplus_{ss}}$ required by a solar

$a_\oplus$ [$\mathrm{mm/s^2}$]	Δt_{AE} [days]	ν_i [deg]	ν_f [deg]	revs.	$a_{\oplus_{ss}}$ [$\mathrm{mm/s^2}$]
1	80.46	280.12	184.46	0	1.1003
0.9	83.27	278.91	185.74	0	1.0671
0.8	86.67	277.46	187.27	0	1.03
0.7	92.32	274.79	189.41	0	0.9751
0.6	112.42	265.34	196.05	0	0.8288
0.5	144.76	251.18	206.14	0	0.6879
0.4	205.56	227.74	223.86	0	0.5581
0.3	389.42	176.22	278.05	0	0.4335
0.2	573.67	247.43	211.1	1	0.2597
0.15	897.04	253.89	153.15	2	0.1862
0.14	934.24	253.31	177.76	2	0.1754
0.13	980.46	247.57	203.78	2	0.1649
0.12	1052.49	232.71	238.94	2	0.1541
0.11	1257.63	170.37	283.47	2	0.1395
0.1	1355	251.63	180.87	3	0.1245
0.09	1463.94	234.42	234.16	3	0.1143

Table 9: Orbit-to-orbit optimal performance for asteroid-Earth transfer phase.

sail to fulfill the same mission. The numerical simulations results are summarized in the last column of Tables 8 and 9.

Note that, the flight time being the same, the characteristic acceleration required by a solar sail is greater than that corresponding to an E-sail, that is, $a_{\oplus_{ss}} > a_\oplus$. This implies that, from the viewpoint of the combination flight time-characteristic acceleration and for this particular mission scenario, an E-sail offers better performance than a solar sail.

6.3.2 Rendezvous constrained transfers

Taking into account the actual position of the two celestial bodies along their orbits, it is possible to calculate the end mission date as a function of the starting date and the waiting time for a given value of the spacecraft characteristic acceleration.

The results of this analysis for $a_\oplus = 0.1\,\mathrm{mm/s^2}$ have been summarized in Fig. 35, which shows the mission end date as a function of the launch window for different values of waiting time ($\Delta t_w \in \{0, 0.5, 1, 1.5, 2\}\,\mathrm{years}$). Note that $\Delta t_w = 0$ corresponds to the limiting case in which the spacecraft performs an asteroid rendezvous and immediately starts the returning flight to Earth. A more interesting mission scenario is obtained when the spacecraft waits around the asteroid for a time interval sufficient to mine the asteroid’s surface and collect the material samples. In this case, assuming $a_\oplus = 0.1\,\mathrm{mm/s^2}$ and a waiting time of about one year, Fig. 35 shows that the whole mission can be fulfilled in slightly less than 11 years.

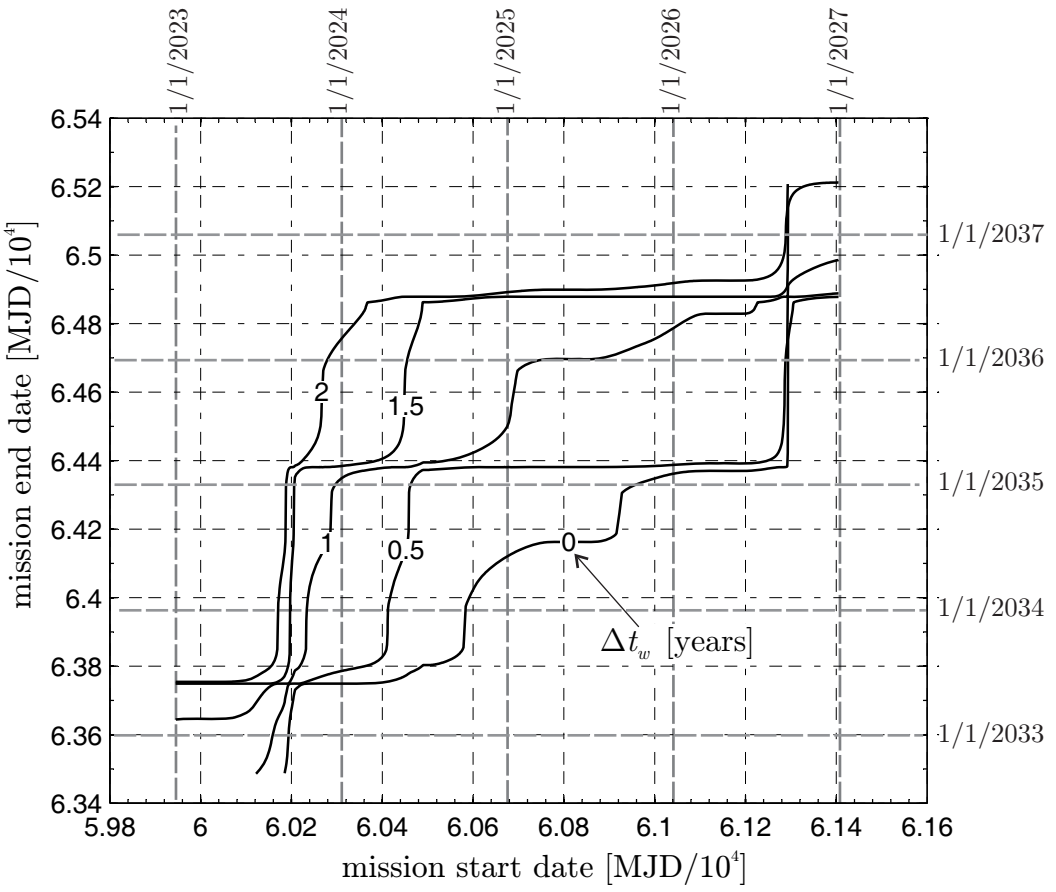

Figure 35: Mission end date as a function of waiting time Δt_w and start date ($a_\oplus = 0.1$ mm/s^2).

7 Generation of artificial equilibrium points

One of the mission scenario in which a propellantless propulsion system exploits its natural potential is for generating and maintaining Artificial Equilibrium Points (AEPs) in a Restricted Three-Body Problem (R3BP) [44]. Indeed, in such a problem the continuous propulsive thrust provided, for example, by an E-sail is able to suitably balance the acceleration resulting from the sum of centrifugal and gravitational forces at a given position.

Here an elliptical restricted problem of the three bodies is considered, where the two main bodies are the Sun and a planet, with the planet moving on an elliptical orbit of eccentricity e and semimajor axis a around the Sun. In such a model the problem of calculating the maps of AEPs position as a function of the E-sail attitude and performance can be addressed in a dimensionless reference frame $\mathcal{T}_p(x/\ell,\, y/\ell,\, z/\ell)$, see Fig. 36 and see Refs. [AD9, AD10, AD11] for more details.

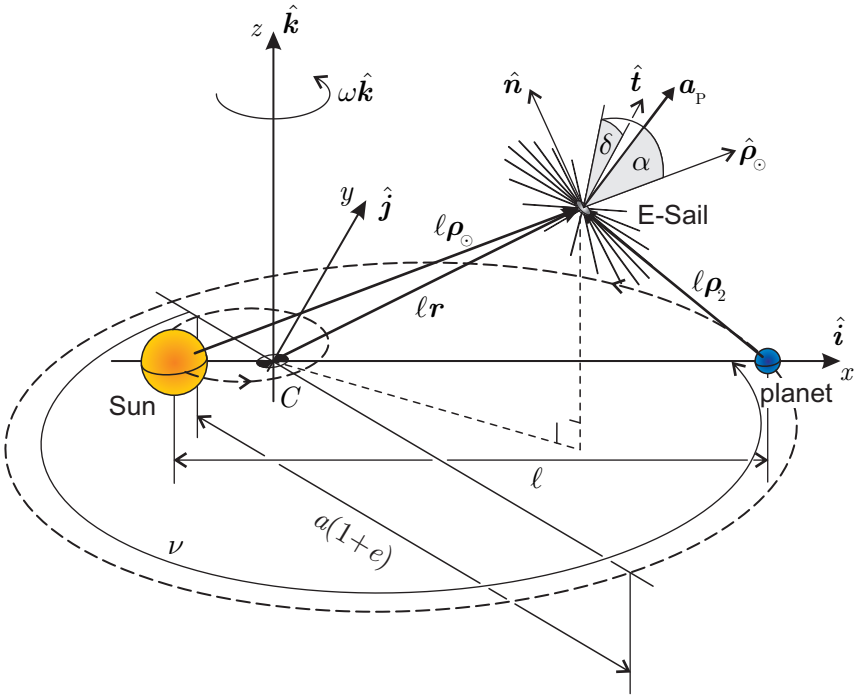

Figure 36: E-sail in the Elliptic Restricted Three-Body Problem.

To avoid the need of a continuous attitude control, the study of AEPs can be performed under the assumption that the sail cone and clock angles are both maintained constant. This means that the direction of $\hat{\boldsymbol{a}}$ remains constant with respect to a $\mathcal{T}_{\mathrm{RTN}}(\hat{\boldsymbol{\rho}}_{\odot},\, \hat{\boldsymbol{t}},\, \hat{\boldsymbol{n}})$ reference frame defined as (see Fig. 36)

$$\hat{\boldsymbol{\rho}}_{\odot} \triangleq \frac{\boldsymbol{\rho}_{\odot}}{\rho_{\odot}} \quad , \quad \hat{\boldsymbol{t}} \triangleq \frac{\hat{\boldsymbol{k}} \times \hat{\boldsymbol{\rho}}_{\odot}}{\|\hat{\boldsymbol{k}} \times \hat{\boldsymbol{\rho}}_{\odot}\|} \quad , \quad \hat{\boldsymbol{n}} \triangleq \hat{\boldsymbol{\rho}}_{\odot} \times \hat{\boldsymbol{t}} \tag{22}$$

Under such assumptions, AEPs are possible only in the plane of motion of the planet provided that the characteristic acceleration defined in Eq. (1) with $d \equiv a$ varies as

$$a_c = a_{c_{\max}} \left(\frac{1 + e\cos\nu}{1+e} \right)^{2-\eta} \tag{23}$$

where ν is the true anomaly of the planet and $a_{c_{\max}}$ is the maximum value of a_c calculated as function of the AEP position.

7.1 Artificial equilibrium points in the Sun-(Earth+Moon) system

Figure 37 shows the propulsive performance required to generate an AEP in a region close to the classical Lagrange point L_1 for the Sun-(Earth+Moon) system, assuming $\eta = 1$. The solid lines represent the isocontour lines of the maximum characteristic acceleration necessary to maintain an AEP, see Eq. (23), and dashed lines correspond to isocontour lines of the (required) sail cone angle α_0. The shaded region highlights the set of AEPs achievable with a sail cone angle $\alpha_0 \leq 30\,\mathrm{deg}$. Because the propulsive acceleration direction must belong to the plane of motion of the attractors, the set of admissible values for δ_0 is restricted to be either $0\,\mathrm{deg}$ (when $y/\ell > 0$) or $180\,\mathrm{deg}$ (when $y/\ell < 0$).

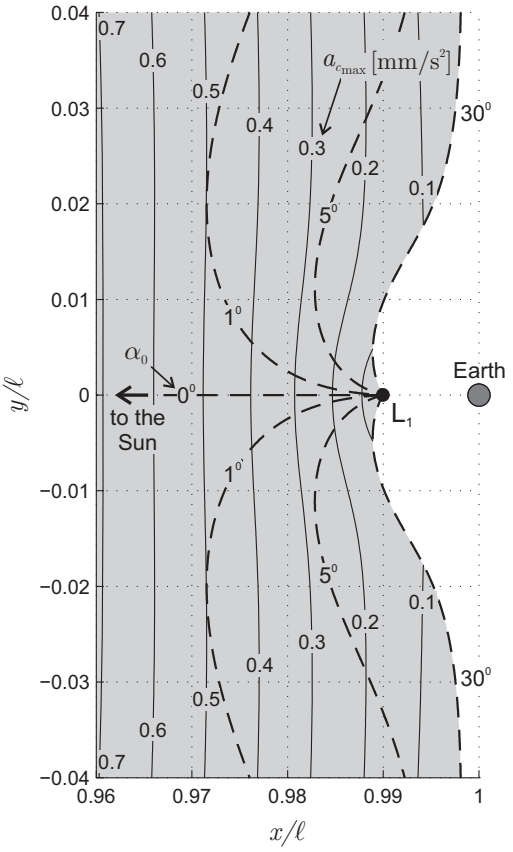

Figure 37: E-sail performance for AEPs close to L_1 in the Sun-(Earth+Moon) system, with $\delta_0 = 0\,\mathrm{deg}$ when $y/\ell > 0$ and $\delta_0 = 180\,\mathrm{deg}$ when $y/\ell < 0$.

Note that positions in Fig. 37 are given in dimensionless form. Actually each fixed position $[\boldsymbol{r}_0]_{\mathcal{T}_p} = [(x/\ell)_0,\, (y/\ell)_0,\, 0]^{\mathrm{T}}$ is in the dimensional reference frame $\mathcal{T}(x,\, y,\, z)$ a segment of length $2\,a\,e\,\|\boldsymbol{r}_0\|$, parallel to the direction of $\boldsymbol{r}_0$, along which the spacecraft oscillates back and forth with a period equal to the Earth's revolution period.

This behavior is better understood when the motion of an E-sail based spacecraft is simulated over a time span equal to the Earth's revolution period. Figure 38(a) shows the trajectory tracked in the frame $\mathcal{T}(x,\, y,\, z)$ by an AEP located at $(x/\ell)_0 = 0.98$ and $(y/\ell)_0 = 0.01$. The dimensional position of the E-sail is expressed in astronomical unit (au). The E-sail oscillates synchronously to the Earth, moving back and forth along the segment PA during a revolution of the Earth around the Sun and reaches the point P (A) when the Earth is at its perihelion (aphelion). The equilibrium conditions for the point in the figure impose that $\alpha_0 = 2.85\,\mathrm{deg}$, $\delta_0 = 0\,\mathrm{deg}$ and that

a_c varies as a function of Earth’s true anomaly as illustrated in Fig. 38(b). Note that $a_{c_{\max}} \approx 0.3295\,\mathrm{mm/s^2}$, which is in agreement with Fig. 37.

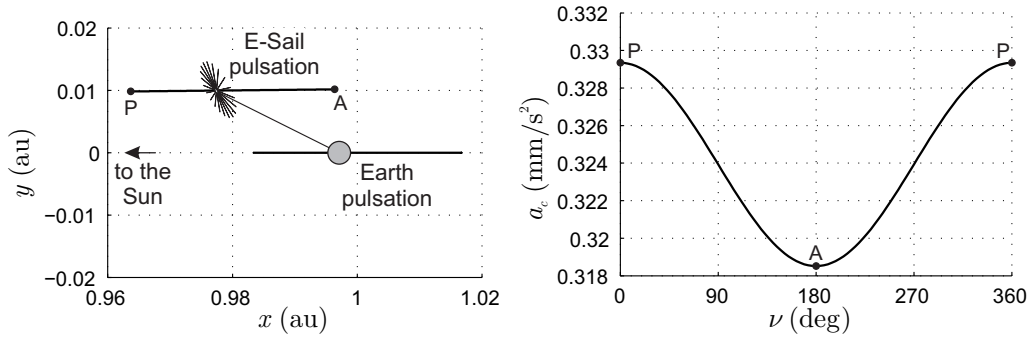

(a) AEP oscillation (b) a_c variation

Figure 38: Trajectory and a_c variation for the AEP located at $(x/\ell)_0 = 0.98$ and $(y/\ell)_0 = 0.01$ in the Sun-(Earth+Moon) system.

7.2 Stability of artificial equilibrium points

A linear stability analysis of the motion in the neighborhood of AEPs shows that regions in the $x - y$ plane exist where the AEPs are stable, see Fig. 39.

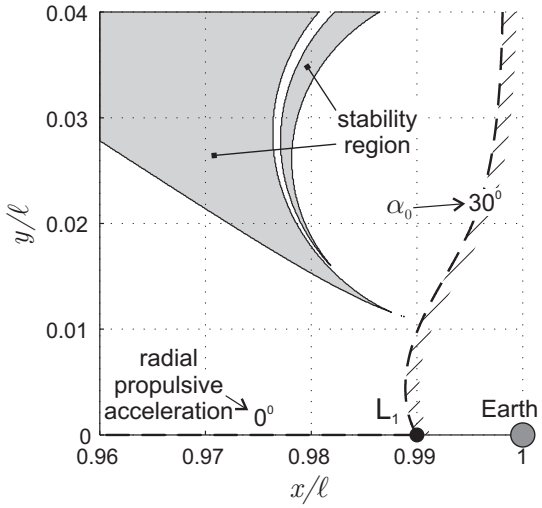

Figure 39: Stability regions close to the classical equilibrium points L_1 in the Sun-(Earth+Moon) system.

Results of Fig. 39 are also confirmed by simulations of the complete dynamics of an E-sail based spacecraft in the three-body problem. Figure 40 shows, as an example, the perturbed trajectories of the spacecraft at two different AEPs. The time interval corresponding to the stable trajectory is 5 years, while for the unstable trajectory it is less than 2 years.

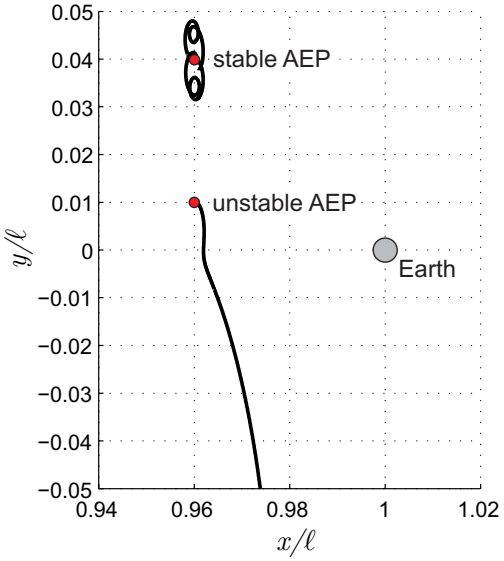

Figure 40: Perturbed trajectories of AEPs in the Sun-(Earth+Moon) system.

8 Conclusions

Extensive orbit analysis and calculations for E-sail based spacecraft missions supporting WP 61 have been developed, whose details are published in peer-reviewed articles [AD2, AD3, AD4, AD5, AD6, AD7, AD8, AD9, AD10, AD11, AD12]. E-sails have shown their suitability as primary propulsion system in several mission scenarios.

In case of missions toward the boundaries of the Solar System, it has been found that a medium-performance E-sail, with a characteristic acceleration of $1.5\,\mathrm{mm/s^2}$, may reach a distance of $100\,\mathrm{au}$ in about $15\,\mathrm{years}$. This means, on one side, that E-sails represent promising alternatives to solar sails. Also, they offer a realistic option for a complex and long term mission such as the IHP mission.

Missions toward both the inner and the outer planets of the Solar System have been simulated for a hybrid E-sail-chemical system. The simulations have shown that the combined use of an E-sail with a chemical thruster is capable of reducing the amount of propellant required to accomplish a given mission transfer, especially for the giant planets and Mercury. The reduction of propellant mass can be translated into a corresponding increase of dry mass fraction deliverable provided that the E-sail mass fraction is less than a critical value. As far as Mercury is concerned, a rendezvous mission with an E-sail provides a conveniently short flight time, even though not as short as that with a pure chemical transfer using a Hohmann strategy. However it is much shorter than what typical gravity assist trajectories can provide. For Venus and Mars, modest propellant savings in comparison to a Hohmann transfer are possible using an E-sail alone or a hybrid solution. For the outer planets, the hybrid solution provides flight time shorter than those required by a direct Hohmann transfer combined with very modest total chemical propulsion ΔV requirements.

A thoroughly investigation of the potentialities of E-sails for mission toward asteroids has been conducted. A total of 1025 missions toward PHA have been studied, showing that with a characteristic acceleration of $1\,\mathrm{mm/s^2}$, about 67% of the PHA may be reached within one year of mission time, and 137 within six months. Although these results have been obtained without taking into account the actual ephemeris constraints, nevertheless they clearly show the potentialities of an E-sail as a primary propulsion system for these mission scenarios. A detailed comparison with a solar sail for a missions toward asteroid 99942 Apophis has been conducted. From the results obtained, the E-sail appears to be an suitable alternative to a solar sail. A preliminary estimate of the performance for nodal flyby missions toward NEAs have shown that most asteroids can be reached within reasonable mission times, and over 60% of NEA population requires a total mission time less than 100 days. By choosing the asteroid 1998 KY-26 as a significant candidate for a possible E-sail based mission, it has been shown that a whole round trip mission, including a suitable scientific phase around the asteroid, can be successfully fulfilled with an E-sail of modest performance.

The existence and stability of AEPs for an E-sail based spacecraft have been investigated within an elliptical R3BP under the assumption of constant orientation of the sail nominal plane. The acceleration required to generate AEPs in the neighborhood of the L_1 point in the Sun-(Earth+Moon) system are compatible with the capabilities of a first order generation E-sail propulsion system. The amount of propulsive acceleration variation, which depends on the true anomaly of the Planet, is moderate and may be compensated through a suitable variation of the tethers' voltage. A linear stability analysis for the Sun-(Earth+Moon) system has shown the existence of stable regions of AEP close to the classical equilibrium points L_1. These points are therefore suitable candidate for scientific missions of spacecraft propelled by an E-sail.

List of Figures

List of Tables

List of Acronyms

2D Two-Dimensional

3D Three-Dimensional

AEP Artificial Equilibrium Point

DT Direct Transfer

E-sail Electric Solar Wind Sail

IHP Interstellar Heliopause Probe

MJD Modified Julian Date

NEA Near-Earth Asteroid

OSIRIS-REx Origins-Spectral Interpretation-Resource Identification- Security- Regolith Explorer

PHA Potentially Hazardous Asteroid

R3BP Restricted Three-Body Problem

SS Solar System

SWA Solar Wind Assist

References

[1] P. Janhunen, “Electric sail for spacecraft propulsion,” *Journal of Propulsion and Power*, vol. 20, pp. 763–764, July-August 2004.

[2] C. R. McInnes, *Solar sailing: technology, dynamics and mission applications*. Springer-Praxis Series in Space Science and Technology, Springer-Verlag, 1999. ISBN: 1-852-33102-X.

[3] R. H. Frisbee, “Advanced space propulsion for the 21st century,” *Journal of Propulsion and Power*, vol. 19, pp. 1129–1154, November–December 2003.

[4] P. Janhunen and A. Sandroos, “Simulation study of solar wind push on a charged wire: basis of solar wind electric sail propulsion,” *Annales Geophysicae*, vol. 25, pp. 755–767, March 2007.

[5] G. Mengali, A. A. Quarta, and P. Janhunen, “Electric sail performance analysis,” *Journal of Spacecraft and Rockets*, vol. 45, pp. 122–129, January–February 2008.

[6] P. Janhunen, P. K. Toivanen, J. Polkko, S. Merikallio, P. Salminen, E. Haeggström, H. Seppänen, R. Kurppa, J. Ukkonen, S. Kiprich, G. Thornell, H. Kratz, L. Richter, O. Krömer, R. Rosta, M. Noorma, J. Envall, S. Lätt, G. Mengali, A. A. Quarta, H. Koivisto, O. Tarvainen, T. Kalvas, J. Kauppinen, A. Nuottajärvi, and A. Obraztsov, “Electric solar wind sail: toward test missions,” *Review of Scientific Instruments*, vol. 81, pp. 111301–1–11301–11, November 2010.

[7] J. E. Prussing and V. L. Coverstone-Carroll, “Constant radial thrust acceleration redux,” *Journal of Guidance, Control, and Dynamics*, vol. 21, pp. 516–518, May-June 1998.

[8] N. Markopoulos, “Analytically exact non-keplerian motion for orbital transfers,” in *AIAA/AAS Astrodynamics Conference*, (Scottsdale, AZ), August, 1–3 1994. Paper AIAA-1994-3758.

[9] A. E. Petropoulos and J. A. Sims, “A review of some exact solutions to the planar equations of motion of a thrusting spacecraft,” in *2nd International Symposium on Low-Thrust Trajectory (LoTus-2)*, (Toulouse, France), June, 18–20 2002.

[10] C. R. McInnes, “Orbits in a generalized two-body problem,” *Journal of Guidance, Control, and Dynamics*, vol. 26, pp. 743–749, September–October 2003.

[11] E. E. Wiesel and S. Alfano, “Optimal many-revolution orbit transfer,” *Journal of Guidance, Control, and Dynamics*, vol. 8, pp. 155–157, January-February 1985.

[12] S. Alfano and J. D. Thorne, “Circle-to-Circle Constant-Thrust Orbit Raising,” *Journal of the Astronautical Sciences*, vol. 42, pp. 35–45, January–March 1994.

[13] R. H. Battin, *An Introduction to the Mathematics and Methods of Astrodynamics*, p. 418. AIAA Education Series, New York: AIAA, 1987. ISBN: 1-563-47342-9.

[14] R. A. Wallace, J. A. Ayon, and G. A. Sprague, “Interstellar probe mission/system concept,” in *Aerospace Conference Proceedings, 2000 IEEE*, vol. 7, (Big Sky, MT), pp. 385–396, Paper no. 53, March 2000.

[15] V. Lappas, M. Leipold, A. Lyngvi, P. Falkner, H. Fichtner, and S. Kraft, “Interstellar heliopause probe: System design of a solar sail mission to 200 au,” in *AIAA Guidance, Navigation, and Control Conference and Exhibit*, (San Francisco, CA), AIAA Paper 2005–6084, August 15–18 2005.

[16] A. E. Lyngvi, M. L. van den Berg, and P. Falkner, “Study overview of the interstellar heliopause probe,” Tech. Rep. 3 (revision 4), ESA, 17 April 2007. reference: SCI-A/2006/114/IHP. `http://esagrid.esa.int/science-e/www/object/index.cfm?fobjectid=40926`.

[17] C. G. Sauer, Jr., “Solar sail trajectories for solar polar and interstellar probe missions,” in *AAS/AIAA Astrodynamics Specialist Conference*, AAS Paper 99-336, August 1999.

[18] P. Janhunen and A. Sandroos, “Increased electric sail thrust through removal of trapped shielding electrons by orbit chaotisation due to spacecraft body,” *Annales Geophysicae*, vol. 27, pp. 3089–3100, August 2009.

[19] P. Falkner, M. L. van de Berg, D. Renton, A. Atzei, A. Lyngvi, and A. Peacock, “Update on esa’s technology reference studies,” (Fukuoka, Japan), 56th International Astronautical Congress, 2005. Paper IAC-05-A3.2A.07.

[20] A. Lyngvi, P. Falkner, S. Kemble, M. Leipold, and A. Peacock, “The interstellar heliopause probe,” *Acta Astronautica*, vol. 57, pp. 104–111, April 2005.

[21] M. Leipold and M. Götz, “Hybrid photonic/electric propulsion,” Tech. Rep. SOL4-TR-KTH-0001, Kayser-Threde GmbH, Munich, Germany, January 2002. ESA contract No. 15334/01/NL/PA.

[22] G. Mengali and A. A. Quarta, “Trajectory design with hybrid low-thrust propulsion system,” *Journal of Guidance, Control, and Dynamics*, vol. 30, pp. 419–426, March–April 2007.

[23] G. Mengali and A. A. Quarta, “Solar-sail-based stopover cyclers for cargo transportation missions,” *Journal of Spacecraft and Rockets*, vol. 44, pp. 822–830, July–August 2007.

[24] R. W. Farquhar, D. W. Dunham, and J. V. McAdams, “NEAR mission overview and trajectory design,” *Journal of the Astronautical Sciences*, vol. 43, pp. 353–371, October-December 1995.

[25] D. Qiao, H. Cui, and P. Cui, “Evaluating accessibility of near-earth asteroids via earth gravity assists,” *Journal of Guidance, Control, and Dynamics*, vol. 29, pp. 502–505, March-April 2006.

[26] R. W. Farquhar, D. W. Dunham, and J. V. McAdams, “Comment on “evaluating accessibility of near-earth asteroids via earth gravity assists”,” *Journal of Guidance, Control, and Dynamics*, vol. 29, pp. 1485–1485, November-December 2006.

[27] M. Morimoto, H. Yamakawa, M. Yoshikawa, M. Abe, and H. Yano, “Trajectory design of multiple asteroid sample return missions,” *Advances in Space Research*, vol. 34, pp. 2281–2285, 2004.

[28] J. V. McAdams, “Postlaunch contingency trajectories for the near-earth asteroid rendezvous mission,” *Journal of Guidance, Control, and Dynamics*, vol. 20, pp. 819–823, July-August 1997.

[29] B. Dachwald and W. Seboldt, “Solar sailcraft of the first generation mission applications to near-Earth asteroids,” in *54th International Astronautical Congress*, (Bremen, Germany), IAC-03-Q.5.06, September–October 2003.

[30] B. Dachwald and W. Seboldt, “Multiple near-earth asteroid rendezvous and sample return using first generation solar sailcraft,” *Acta Astronautica*, vol. 57, no. 11, pp. 864–875, 2005.

[31] B. Dachwald and B. Wie, “Solar sail kinetic energy impactor trajectory optimization for an asteroid-deflection mission,” *Journal of Spacecraft and Rockets*, vol. 44, pp. 755–764, July–August 2007.

[32] G. Mengali and A. A. Quarta, “Rapid solar sail rendezvous missions to asteroid 99942 Apophis,” *Journal of Spacecraft and Rockets*, vol. 46, pp. 134–140, January–February 2009.

[33] D. F. Bender and R. D. Bourke, “Multiasteroid comet missions using solar electric propulsion,” *Journal of Spacecraft and Rockets*, vol. 10, pp. 481–482, August 1973.

[34] G. Mengali and A. A. Quarta, “Optimal missions with minimagnetospheric plasma propulsion,” *Journal of Guidance, Control, and Dynamics*, vol. 29, pp. 209–212, January–February 2006.

[35] G. Mengali and A. A. Quarta, “Minimagnetospheric plasma propulsion for outer planet missions,” *Journal of Guidance, Control, and Dynamics*, vol. 29, pp. 1239–1242, September–October 2006.

[36] R. L. Schweickart, “Decision program on asteroid threat mitigation,” *Acta Astronautica*, vol. 65, pp. 1402–1408, November-December 2009.

[37] J. L. Remo, “A quantitative NEO hazard mitigation scale,” *Acta Astronautica*, vol. 54, pp. 755–762, May 2004.

[38] D. J. Korsmeyer, R. R. Landis, and P. A. Abell, “Into the beyond: A crewed mission to a near-earth object,” *Acta Astronautica*, vol. 63, pp. 213–220, July-August 2008.

[39] A. Phipps, M. Meerman, J. Wilhelm, D. Gibbon, J. Northam, A. da Silva Curiel, J. Ward, and M. Sweeting, “An ‘entry level’ mission to a near earth object,” *Acta Astronautica*, vol. 59, pp. 845–857, October-December 2006.

[40] E. Perozzi, A. Rossi, and G. B. Valsecchi, “Basic targeting strategies for rendezvous and flyby missions to the near-earth asteroids,” *Planetary and Space Science*, vol. 49, pp. 3–22, January 2001.

[41] G. W. Hughes and C. R. McInnes, “Small-body encounters using solar sail propulsion,” *Journal of Spacecraft and Rockets*, vol. 41, pp. 140–150, January-February 2004.

[42] E. M. Standish, “JPL planetary and lunar ephemerides, DE405/LE405,” Interoffice Memoradum IOM 312.F-98-048, Jet Propulsion Laboratory, August 26 1998. http://iau-comm4.jpl.nasa.gov/de405iom/de405iom.pdf.

[43] E. M. Standish, “The observational basis for JPL’s DE200, the planetary ephemerides of the astronomical almanac,” *Astronomy and Astrophysics*, vol. 233, pp. 252–271, July 1990.

[44] R. J. McKay, M. Macdonald, J. Biggs, and C. McInnes, “Survey of highly-non-keplerian orbits with low-thrust propulsion,” *Journal of Guidance, Control, and Dynamics*, vol. 34, pp. 645–666, May-June 2011.